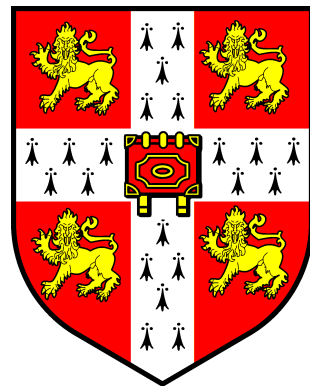


SIMULATION OF BREATHING FOR MEDICAL APPLICATIONS

Thierry Josua Maldonado

Hughes Hall

UNIVERSITY OF CAMBRIDGE



Department of Engineering
Signal Processing and Communications Laboratory

A dissertation submitted to the
UNIVERSITY OF CAMBRIDGE
for the degree of
MASTER OF PHILOSOPHY

July 2011

Preface

The research described in this thesis was carried out between October 2010 and July 2011. The work presented is part of a Master of Philosophy project under Dr Joan Lasenby's supervision within the Signal Processing and Communications Laboratory, Department of Engineering, University of Cambridge.

Declaration

This thesis is the result of my own work and includes nothing which is the outcome of the work done in collaboration, except where specifically indicated in the text. No part of this dissertation has previously been submitted for any similar qualification or degree. The thesis contains no more than 15,000 words excluding figures, tables, footnotes and the appendix.



Thierry J. Maldonado

Published work

This work was presented during the 2011 edition of the *Exciting Research in Information Engineering Conference* of the Cambridge University Engineering Department as a poster and won the Best Poster Award.

The work was also presented at SIGGRAPH 2011 Vancouver [1] and has been retained for the semi-finals of the ACM Student Research Competition.

Copyright

This thesis is copyright Thierry J. Maldonado, 2011. All rights reserved. No part of this publication may be reproduced stored in a retrieval system, or transmitted, in any form or by any means, electronic, mechanical, photocopying, recording, or otherwise, without prior permission.

All statements in this work are believed to be true and accurate at the time of its production but neither the author nor the University of Cambridge offer any warranties or representations nor can they accept any legal liability for errors or omissions.

Composition of the jury

This thesis was defended on the 23rd of September 2011 in front of the jury composed of:

Professor Isabelle Bloch, Télécom ParisTech

External examiner

Professor Richard W. Prager, University of Cambridge

Internal examiner

Simulation of Breathing for Medical Applications

Thierry J. Maldonado

This work describes further research on the Structured Light Plethysmography (SLP) project [2] which is a non-invasive method for pulmonary function testing using visible light. This technique uses two cameras and a known grid which is projected onto the chest of a patient. Using stereo vision algorithms, the 3D coordinates of each grid point projected on the chest wall are recovered over time. As the device captures only the front of the chest wall, we cannot infer the absolute volumes of the lungs but only volume changes of the thoracic cage. However, when it comes to examining respiratory function in a patient, absolute volumes represent a crucial piece of information. In order to address this problem we use optimisation techniques to fit SLP data to a highly detailed 3D model of the human torso (composed of rigid parts and muscles) that we have created. Our simulation provides us with both the optimal muscle inputs to simulate breathing and the absolute volumes of the lungs for a given SLP dataset. As we wish to investigate pulmonary function, the model must be anatomically and physiologically accurate enough to be medically approved. Previous attempts have concentrated more on the visual side of the simulations than on the medical applications, which often resulted in overly simplified models. Lee et al. [3] describes a model of the whole upper body but with few respiratory muscles of the rib cage and with no diaphragm, which is an essential muscle in breathing. Zordan et al. [4] uses a skeleton model which anatomically-wise lacks realism and simplifies the articular bones in the spine and the rib cage by grouping and treating them as a single rigid body. Furthermore, in [4] the different muscles are grouped and receive the same input (a step function for the diaphragm and sine functions for all the others) in order to produce visually pleasing results. In comparison, our model has high anatomical accuracy in the dimensions of the rigid parts and in the locations of the joints linking them and the muscles involved in breathing (the rigid parts, the joints and the muscle locations were designed using current anatomy books). In addition, it has high-level controls, is fully tunable (each muscle can be activated independently) and can be fitted to different patient anatomies. The results obtained from our simulations through our data-driven approach were compared with the data from another conventional lung volume measuring technique, spirometry. Both frequentist and Bayesian tests were used to compare the datasets.

Table of Contents

List of Figures	viii
List of Tables	ix
Introduction	1
1. Human Torso Model	5
1.1. Related work	5
1.2. Breathing mechanisms	7
1.3. Rigid-body components	9
1.3.1. Spine	10
1.3.2. Thoracic cage	10
2. Respiratory Muscles Simulation	15
2.1. Spring muscle element	15
2.2. Rib cage	16
2.2.1. Intercostal muscles	16
2.2.2. Scalene muscles	17
2.3. Abdominal cavity	19
2.4. Control of the model	21
2.4.1. Chest breathing	23
2.4.2. Abdominal breathing	24
3. Fitting Datasets to the Model	27
3.1. Structured Light Plethysmography datasets	28
3.2. Adapting a skin mesh	29
3.3. Skinning deformation	31
3.4. Fitting of SLP datasets	33

Table of Contents

4. Validation of the Simulation	37
4.1. Experiment set up	37
4.2. Preparing the data for comparison	39
4.3. Optimisation process and data analysis	40
4.3.1. Performances of the optimisation	40
4.3.2. Analysis of the optimisation outputs	42
Phase shift between the abdominal and rib cage cavities	43
Relative contributions from the abdominal and rib cage cavities	44
4.4. Comparing simulation and spirometry data	45
4.4.1. Correlation coefficient	46
4.4.2. The Bland-Altman plot	46
4.4.3. The cosinor model	48
4.4.4. BARS: Bayesian Adaptive Regression Splines	50
5. Implementation Issues	55
5.1. Joints and muscles	55
5.2. Abdominal movement	57
5.3. Optimisation	57
Conclusion	59
A. Simulation and Spirometry Data	61
A.1. Subject 1	62
A.2. Subject 2	63
A.3. Subject 3	64
B. Bland-Altman Plots for Simulation and Spirometry Data	65
B.1. Subject 1	66
B.2. Subject 2	67
B.3. Subject 3	68
Bibliography	69

List of Figures

1.1.	Respiratory system in action	8
1.2.	Skeleton model used	9
1.3.	Comparison of true and simulated spine	11
1.4.	The different parts of an individual rib and its articulations	13
1.5.	Comparison with the simulated rib cage	14
2.1.	Intercostal muscles	17
2.2.	Effects of rib curvature on the net moment exerted by an intercostal muscle . .	18
2.3.	Simulation of the external intercostal the internal intercostal muscles	18
2.4.	Comparison with the simulated scalene muscles	19
2.5.	Sketch of how the abdomen assists in breathing	20
2.6.	The abdominal muscles	20
2.7.	Simulation of the abdominal cavity muscles involved in breathing	21
2.8.	Simulation of the abdominal cavity	22
2.9.	Activation functions of the different muscles for a plausible simulation	25
3.1.	Diagram of the Structured Light Plethysmography device	28
3.2.	SLP in action	29
3.3.	Personalised skin meshes derived according to physiognomy data	29
3.4.	The process of fitting a skin mesh	32
3.5.	Skin weights of the fitted skin mesh	33
3.6.	SLP-driven system overview	34
3.7.	Simulated lungs' volume for the same subject breathing in different positions .	36
4.1.	Experiment set up	38
4.2.	Preparation of the simulation and spirometry data before comparison	41
4.3.	Bland-Altman plots for spirometry and simulation data	47
4.4.	Simulation and spirometry data and the corresponding cosinor fits	49
4.5.	Simulation and spirometry data and the corresponding BARS fits	51

List of Figures

5.1. Comparison with the simulated spine	56
5.2. Implementation structure of the optimisation process	58
A.1. Simulation and spirometry data from subject 1	62
A.2. Simulation and spirometry data from subject 2	63
A.3. Simulation and spirometry data from subject 3	64
B.1. Bland-Altman plots for simulation and spirometry data from subject 1	66
B.2. Bland-Altman plots for simulation and spirometry data from subject 2	67
B.3. Bland-Altman plots for simulation and spirometry data from subject 3	68

List of Tables

1.1.	Body masses	14
3.1.	Control parameters derived from the same subject in different positions	35
4.1.	Subjects's anatomy data	39
4.2.	Improvement provided by the skin fitting process over the skin error	42
4.3.	Optimal parameters found for the different datasets	43
4.4.	Results of the correlation, cosinor and BARS methods	54

Introduction

On average, an adult breathes 10,000 litres of air a day providing oxygen to the body that is essential for human life. However, it is not well known that respiratory diseases are the leading cause of death worldwide. According to the European Lung Foundation, in terms of mortality, incidence, prevalence and costs, respiratory diseases rank second after cardiovascular diseases. In some countries (e.g. the UK), they are in fact the leading killer. Respiratory diseases affect all subsets of the population independent of age and sex; even animals are affected. To detect, understand and cure respiratory diseases it is crucial to assess the respiratory status of a patient. This is mostly achieved with the knowledge of the volume changes of the lungs with time. Current techniques are mostly invasive in the sense that they require the patient's cooperation and physical interaction with some device. Up to now, the most commonly performed technique has been *spirometry* which involves the patient blowing into a mouthpiece to produce flow versus time from which volume changes in the lungs can be inferred. While spirometry provides accurate results, as it is an invasive device, various subsets of the human population, such as babies and the elderly, are unable to use it. There have been recent advances in the design of non-invasive technologies, such as the elastomeric plethysmograph (piezoelectric belt fastened around a patient's chest which gives the volume change of the chest according to deformations of the belt) or the opto-electronic plethysmograph (optical reflectance motion-analysis system that measures the volume change of the chest wall by computing 3D coordinates of markers placed on the rib cage and abdomen). However, the elastomeric plethysmograph suffers from artefacts due to inevitable changes in body position and the opto-electronic plethysmograph is still very expensive and requires a big space that is not available in most hospitals.

This report outlines further research on the Structured Light Plethysmography (herein abbreviated as SLP) project which is a non-invasive method for pulmonary function testing using visible light. This technique uses two cameras and a known grid which is projected onto the chest of a patient. Using stereo vision algorithms, a surface approximation of the chest wall moving over time is reconstructed. As the device captures only the front of the chest wall, we cannot infer the absolute volumes of the lungs but only volume changes of the thoracic cage (in our case, using Gauss's Theorem). However, when it comes to examining respiratory function

Introduction

in a patient, absolute volumes represent a crucial piece of information. In order to address this problem we have created a realistic 3D model of the chest and abdomen, together with a muscle structure which can be activated to produce movement, and a skin which represents the torso surface. The idea is to create breathing via time variation of a small number of parameters (basically muscle activations). We can then fit our observed data to our moving model—this will give us the parameters of the model and from these we can infer the volume changes in the lungs. In addition, we will produce a better visualisation of the respiratory movements. The project therefore consists of modelling the different parts of the human body responsible for respiration and controlling the model by fitting data from the SLP system.

There are six distinct steps in this project:

1. Understand the respiratory system and the breathing movements.
2. Model the rib cage (bones and muscles) and simulate movement.
3. Model the diaphragm and synchronise its movement to the rib cage.
4. Rig an adapted skin mesh to the rib cage and diaphragm models.
5. Fit the data from the SLP to the model.
6. Validate our method by comparing the results obtained with different well-acknowledged techniques.

As complex interactions occur inside the human torso between rigid parts (e.g. spine, ribs and sternum) and deformable ones (e.g. lungs, abdomen and diaphragm), realistic anatomical modelling of the human torso has been a major challenge in computer animation. Previous attempts were more concentrated on the visual side of the simulations than on the medical applications, which often resulted in overly simplified models.

To summarise, this work makes five primary contributions:

1. We introduce a model which has high anatomical accuracy in both the dimensions of the rigid parts and the locations of the joints linking them.
2. We develop a fully tunable model that can be fitted to different patient anatomies.
3. We present high-level controls that could be used to activate the model to produce different breathing patterns.
4. We design a method relying on optimisation to fit SLP datasets to the simulation.
5. We validate our method by comparing it to a medically well-acknowledged lungs' volume measurement device called spirometry.

The thesis is organised into five chapters as outlined below.

Introduction

Chapter 1 will review relevant prior work on modelling and simulating the human torso, then describe the different mechanisms involved in breathing to finally explain how we modelled the rigid-parts of our simulation.

Chapter 2 will describe the muscle element model we used and explain in detail the muscles responsible for breathing mechanisms and their actions. Finally, it details how these muscles are simulated and activated in the model.

Chapter 3 will provide some relevant background on the SLP technique and the nature of the data it provides. It will then explain how we fit an adapted skin mesh to the model and describe how this skin mesh is deformed according to the rib cage and abdomen motion. Finally, it will detail the optimisation algorithms used to fit the SLP dataset to the model.

Chapter 4 will discuss the validity of our method. Firstly, it will describe the protocol followed to acquire data and provide an analysis of the data obtained on three subjects. Secondly, it will present the different comparison techniques and the results achieved with our datasets.

Chapter 5 will explain how we implemented our method and the different software and file types used.

1

Human Torso Model

Our work is at the border between physical modelling, simulation in computer animation and related areas of interest such as physiology, anatomy, biomechanics and control. This chapter reviews relevant prior work on modelling and simulating the human torso, then describes the different mechanisms involved in breathing in order to explain how we modelled the rigid-parts of our simulation.

1.1. Related work

In previous work, human torso models have been simplified to a few components. For instance, Carranza et al. [5] uses a simple body model based on a triangle mesh shape and a kinematic skeleton. Others, such as Monheit and Badler [6], present a kinematic model of the human spine and torso where the total bending angle is distributed to each joint according to weighting parameters.

Lee et al. [3, 7] describes a detailed model of the whole upper body. The model derives from a musculoskeletal system with 814 Hill-type muscle actuators (a spring and a damper in parallel with another spring) and a coupled finite element simulation of soft tissue deformations. The

skeleton is made of 68 bones. Using a commercial model called the Ultimate Human model [8], the team built the skeletal muscles using piecewise line segments. They omitted the diaphragm and as a result, the respiratory movement is mainly accomplished by the intercostal muscles. However, Konno et al. [9] experimentally found that the abdomen accounted for around half of the tidal volume (volume of air displaced between normal inspiration and expiration) and just less than half of the vital capacity (maximum amount of air a person can expel). As a consequence, the role of the abdomen is absolutely crucial in breathing and its absence in [3, 7] makes the model incomplete in terms of breathing simulation. For model simplification reasons also, some muscles involved in breathing such as the transversus abdominis were avoided too. Special care is taken to model the soft tissue, as the goal sought here is to get a high quality surface representation from the model. To animate the model the authors use a two-step process: first they collect the different positions, orientations and joint angles of the main limbs of the upper body over time—from target key poses or motion capture data—and then they compute the muscle activation levels that have to be applied to the model in order to achieve these positions. Given the positions of the bones and the activation level of each muscle, the soft tissue is deformed according to coupling relations (linking bones and soft tissue, muscle forces and directions). Some simulations of breathing are presented in [3] but the very few respiratory muscles used and the absence of abdominal breathing over-simplify the complex process of breathing and produce good but not totally realistic movements.

The models of the human torso presented by DiLorenzo et al. [10, 11] (known as the Breathe Easy model) and by Veltkamp et al. [12] use both anatomical and physical data to describe breathing. Using spring-based muscles the torso model can be put into motion by stimulating the ribs and the diaphragm (the abdomen and the gut move passively). The simulation also uses estimated pressure forces to preserve the volume of the deformable components such as the gut, which is modelled as a deformable and incompressible volume. They applied different contraction input signals and chose the most visually pleasing ones in their simulations. The authors derived their model from an existing skeleton available at www.3Dcafe.com, a free 3D database platform. However, the origin of the model used is unknown and no validation of its anatomical accuracy has been carried out. In the Breathe Easy model, the skin surface is a NURBS¹ surface based on trace vertices from the skeleton simulation; all the computation is done through the 3D modelling software program Autodesk Maya [13]. The validation of the model involved computing different volumes of the lung cavity of the model during different kind of breathing styles and to compare them to average figures that can be found in the literature. However, the volume curves shown in [10] are not realistic according to [12]. Moreover, as the accompanying video of [10] shows little abdominal breathing, [12] criticises the lack of realism of the simulation.

While [14, 4, 10, 12] present detailed models of the human torso, we note that important simplifications are used and particularly, the articular bones in the spine and the rib cage are grouped and treated as a single rigid body. In addition, the models presented by [4, 10, 12]

¹Non-Uniform Rational B-Spline.

are put into motion by activating groups of muscles evenly, which is a simplification compared to the model we present in later chapters, in which activation inputs are fully tunable.

Finally, the only means of validation used in previous work relied on the plausible shapes of the curves obtained through simulation. In order to validate our method, we compare the simulation data to spirometry data.

1.2. Breathing mechanisms

To understand the different modelling decisions we made to build our torso simulation, we must first understand how humans breathe. This section describes the different breathing mechanisms and uses several medical terms which are defined here:

caudal direction: towards the tail end of the body.

cranial direction: towards the head end of the body.

dorsal direction: the surface directed towards the back or spine.

medial direction: towards the median plane (a vertical plane passing through the body from nose tip to tail tip).

lateral direction: the surface directed away from the median plane.

ventral direction: the surface directed towards the belly or ground.

chondrocostal: pertaining to the ribs and the costal cartilages.

Breathing is the process that moves air in and out of the lungs. The movement of breathing can be split into two distinct steps: inspiration and expiration. Inspiration consists of filling up the lungs with fresh air, rich in oxygen, by expanding the volume inside the chest wall. The oxygen is then transmitted to the blood through lung capillaries and is distributed to the whole body via the circulatory system. Meanwhile, through the same capillaries, the blood passes the carbon dioxide it contains to the air in the lungs. Then, expiration consists of removing the air—now full of carbon dioxide and poor in oxygen—by contracting the chest wall. Thereby, breathing entails expanding and contracting the chest wall. From a physiological point of view, this is done through two different moving parts of the body: the rib cage and the abdominal cavity.

Konno et al. [9], recorded changes in diameter of the rib cage and the abdomen during breathing in six subjects. Motion-wise, it seems that the rib cage and the abdomen each move as a unit and that under a fixed total volume constraint, there is a dependence of motion between the two and a degree of volume independence when this constraint is relaxed. They experimentally constructed relationships between volume displacement and linear motion of

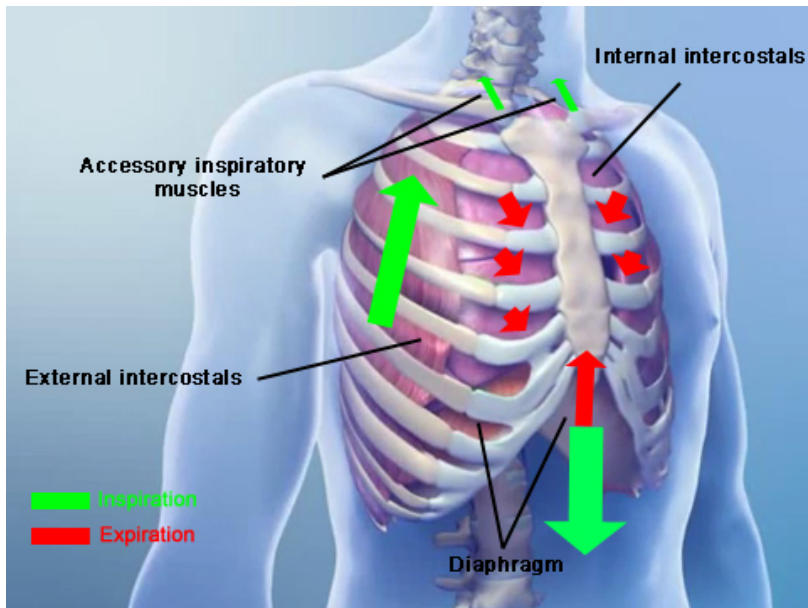


Figure 1.1. Respiratory system in action. Diagram taken from the Biophysics4Arab's Channel.

the abdomen and the rib cage; and applied these relationships to estimate the separate volume changes. During normal breathing, the chest wall is approximated as two moving ‘parts’—the rib cage and the abdomen—in an open system (with two degrees of freedom). As a result, the mechanism of breathing can be split into two independent systems: chest breathing and abdominal breathing.

The respiratory muscles change the volume of the lungs by changing the volume of the thoracic cavity. The inspiratory muscles are the diaphragm, the external intercostal muscles and the accessory muscles (also called the accessory inspiratory muscles). The major expiratory muscles are the internal intercostal muscles and the abdominal muscles (see figure 1.1).

During the inspiration phase of breathing the diaphragm (which is a large and thin muscle, which stretches across the chest under the rib cage separating the abdominal cavity from the chest cavity) contracts and flattens out going downward and expanding the space in the chest. The diaphragm gains its shape from its attachments and the surrounding organs: heart, lungs, and liver. At the same time, the external intercostal muscles contract pulling the rib cage upward and expanding the thoracic cavity (and as a consequence the lungs’ volume). During forceful inspirations, the scalene muscles located in the neck contract to further enlarge the thoracic cavity. As the rib cage expands, the intra-alveolar pressure reduces below the atmosphere pressure. The air is drawn into the lungs until the pressure equilibrates.

During expiration the diaphragm and the intercostal muscles relax and the thoracic cavity and the lungs return to their pre-inspiratory size. As the lungs recoil the intra-alveolar pressure increases above the atmosphere pressure. The air goes out of the lungs until the pressure equilibrates again. No muscles contract during quiet expiratory breathing. However, during forceful expirations, the abdominal muscles and the internal intercostal muscles contract to reduce the

thoracic cavity further than during passive expiration. The abdomen wall is indirectly driven by the pumping of the diaphragm and stores potential energy through inhalation, which could be usable for exhalation.

Interestingly enough, the lungs do not affect the outward appearance of the trunk during regular respiration [4].

1.3. Rigid-body components

As the mechanism of breathing is driven by two different sections of the chest wall, our torso simulation includes three main categories: rigid-body components (e.g. spine, ribs and sternum), soft-body components (e.g. lungs, abdomen and diaphragm) and the muscle elements.

In contrast to DiLorenzo et al. [11] and Veltkamp et al. [12] who used a skeleton from www.3Dcafe.com and Lee et al. [7] who used the commercial Ultimate Human model, we used a skeleton of high anatomical accuracy. The partial skeleton (spine, ribs and sternum) in figure 1.2 was taken from a complete 3D skeleton model constructed by Dr. M. Bobot who used real anatomical data in its construction. We are very grateful for his permission to use this skeleton.

The skeleton, which can be seen in figure 1.2, was kindly given by Dr. M. Bobot who realised it from several anatomy books [15, 16, 17]. From the whole 3D skeleton model, only the vertebrae of the spine, the ribs and the sternum were used.

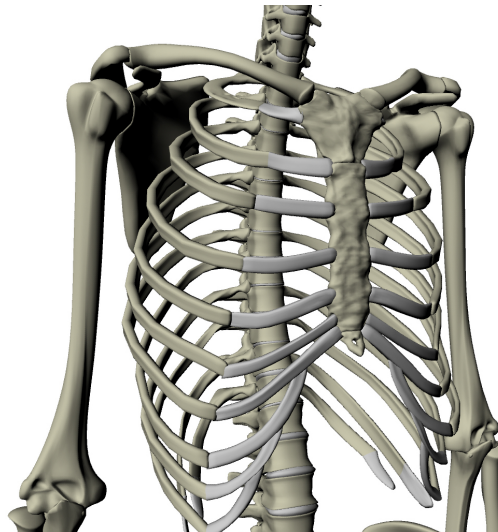


Figure 1.2. Skeleton model used.

1.3.1. Spine

The spine is composed of 24 vertebrae. The different regions of the vertebral column contribute to the skeletal framework of the thorax, abdomen, and pelvis. The number and specific characteristics of the vertebrae vary depending on the body region with which they are associated. There are seven cervical, twelve thoracic, five lumbar, five sacral, and three to four coccygeal vertebrae (see figure 1.3(a)). The spine simulation can be seen in figure 1.3(b).

Between adjacent vertebrae in the spine lies an intervertebral disc. Each disc forms a cartilaginous solid joint to allow slight movement of the vertebrae, and acts as a ligament to hold the vertebrae together. As in [11, 12, 7], we modelled each joint as a ball joint.

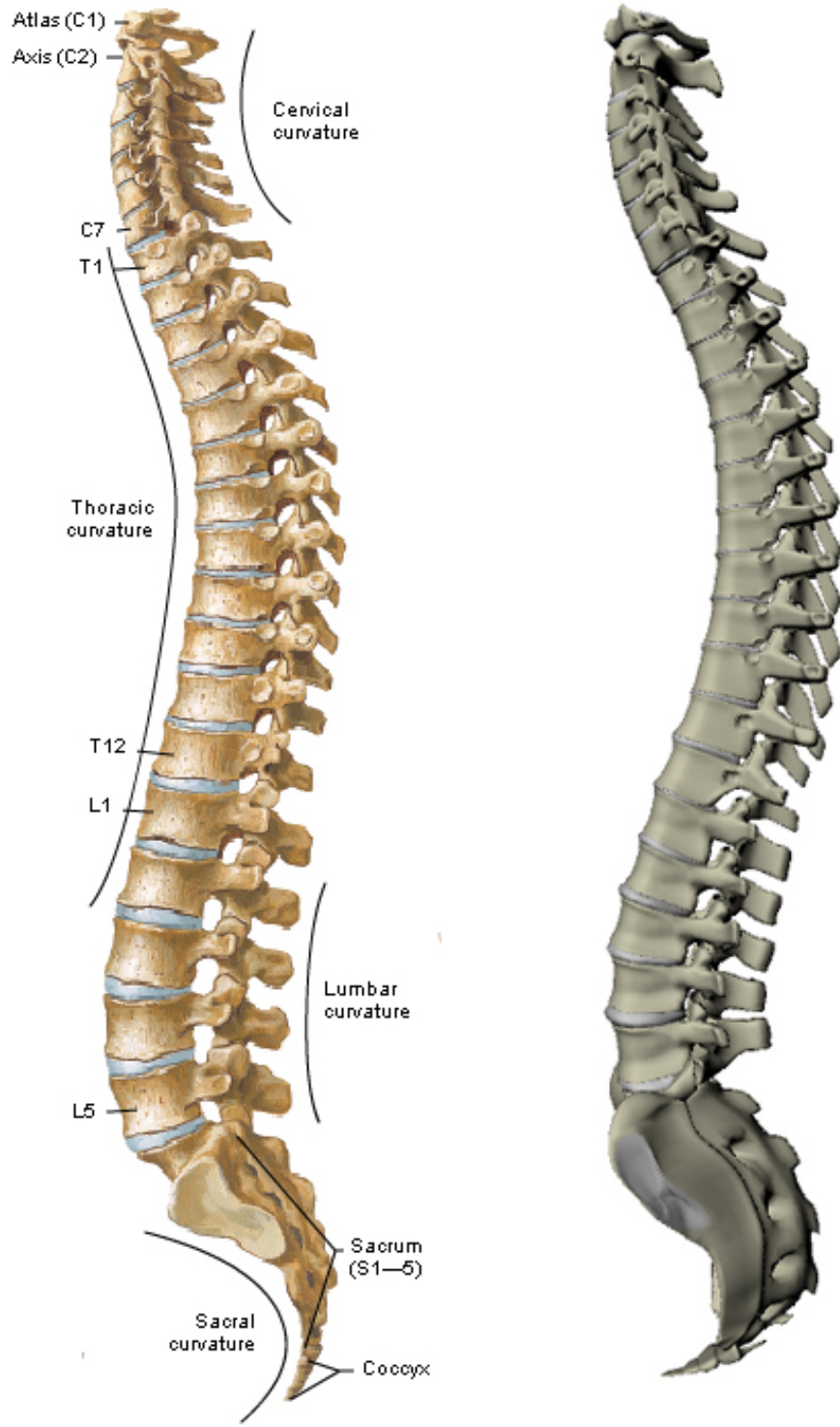
1.3.2. Thoracic cage

Thanks to its shape that provides rigidity, the thoracic cage (rib cage) protects internal structures within the thorax (e.g. heart, great vessels, lungs, and trachea). The thoracic cage includes the sternum, twelve pairs of ribs (numbered from one to twelve, from top to bottom as shown in figure 1.5(a)) and costal cartilages, the twelve thoracic vertebrae and intervening intervertebral discs mentioned in section 1.3.1. Because the thorax area is constantly in motion, it is one of the most dynamic regions of the body. With each breath, the muscles of the thoracic wall work in concert with the diaphragm and muscles of the abdominal wall vary the volume of the thoracic cavity. This is done first by expanding the capacity of the cavity, thereby causing the lungs to expand and draw air in and then, due to lung elasticity and muscle relaxation, decreasing the volume of the cavity and causing the lungs to expel air.

The domed shape of the thoracic cage provides remarkable rigidity, given the light weight of its components, enabling it to:

1. Protect vital thoracic and abdominal organs (heart, great vessels, lungs, and trachea) from external forces.
2. Resist the negative (sub-atmospheric) internal pressures generated by the elastic recoil of the lungs and inspiratory movements.
3. Provide attachment for and support the weight of the upper limbs.
4. Provide the anchoring attachment (origin) of many of the muscles that move and maintain the position of the upper limbs relative to the trunk, as well as provide the attachments for muscles of the abdomen, neck and the back.

The sternum and cartilage that connect to the ribs is a very stiff but deformable material. We approximate cartilage by modelling it as a rigid body. As the global movement between a rib and the sternum are mainly rotations due to the very stiff nature of the cartilage, we modelled the joint between each rib to the sternum with a ball joint. The sternum moves ventrally.



(a) Anatomical vertebral column from [16].

(b) Simulated vertebral column.

Figure 1.3. Comparison of true and simulated spine.

Consequently, there is usually an increase in both the lateral and the dorsoventral diameters of the rib cage during inspiration.

Ribs are curved, flat bones that form most of the thoracic cage as shown in figure 1.4(a). There are three types of ribs:

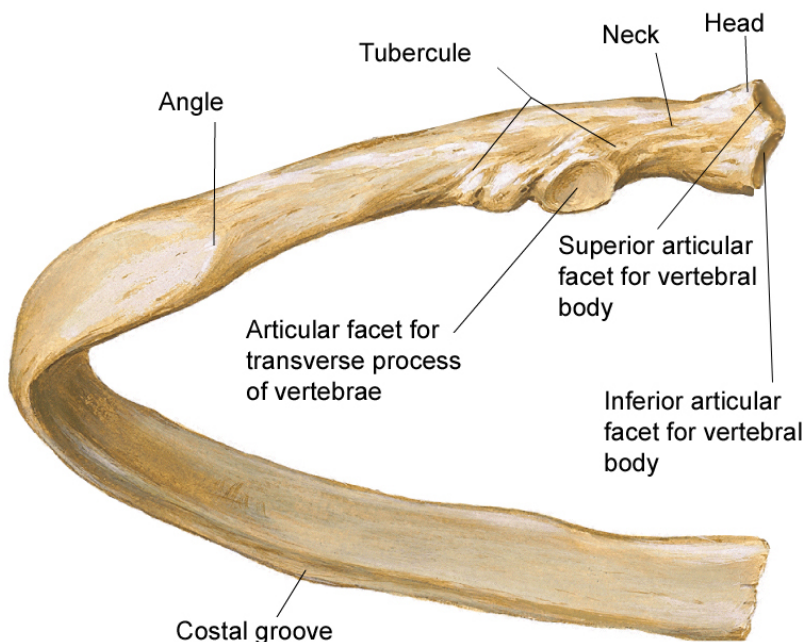
1. True (vertebrocostal) ribs (1st-7th ribs): they attach directly to the sternum through their own costal cartilages.
2. False (vertebrochondral) ribs (8th, 9th, and usually 10th ribs): their cartilages are connected to the cartilage of the rib above them; thus their connection with the sternum is indirect.
3. Floating (vertebral, free) ribs (11th, 12th, and sometimes 10th ribs): the rudimentary cartilages of these ribs do not connect even indirectly with the sternum; instead they end in the posterior abdominal musculature.

The displacements of the rib cage during breathing are essentially due to the motion of the ribs. Each rib is fixed to the spine with two joints: the costovertebral and costotransverse joints, together resulting in a hinge joint in the direction of the rib's neck as shown in figure 1.4(b). When a rib is displaced, its ventral end moves laterally and ventrally as well as cranially. The sternum moves ventrally. Consequently there is usually an increase in both the lateral and the dorsoventral diameters of the rib cage during inspiration.

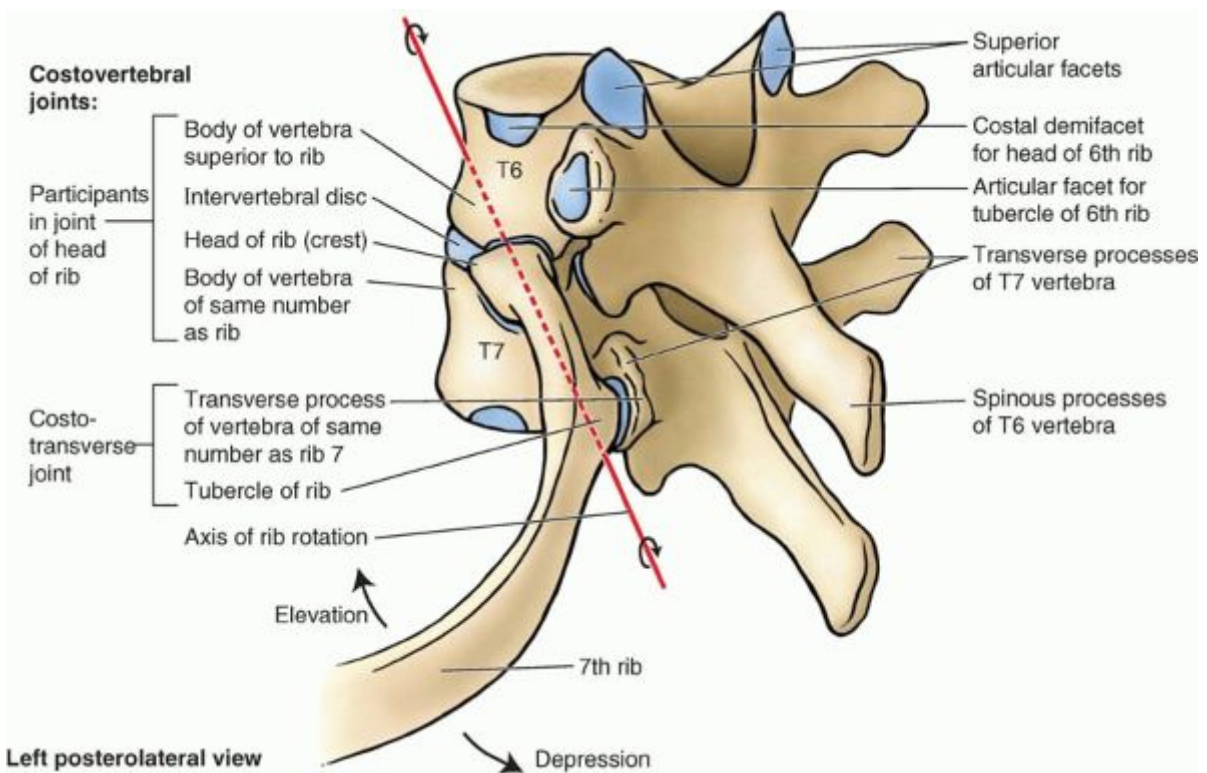
We have assigned physiology based masses to these rigid components of the rib cage using data given by [11] (see table 1.1).

In contrast to [11], who modelled the joints between each rib and the spine with ball joints and [12] who modelled them with hinge joints but only oriented laterally, our modelling is anatomically correct with hinge joints crossing the *articular facet for transverse processes of vertebrae* and the middle of the *superior articular facet for vertebral body* and the *inferior articular facet for vertebral body* of each rib (see figure 1.4).

In figure 1.5 we can see a frontal view of (a) an anatomical rib cage versus (b) our simulated rib cage, versus (c) the simulated rib cage from Breathe Easy [11]. We notice that in the Breathe Easy simulation, the first rib is over curved in the cranial direction and that from the 4th to the 8th rib, the curvature is too high resulting in a rib cage with a wide end.



(a) Rib diagram from [16].



(b) Costovertebral articulations of a typical rib. The rib moves (elevates and depresses) around an axis that traverses the head and the neck of the rib. This axis is oriented laterally, dorsally and caudally. Diagram taken from [18].

Figure 1.4. (a) the different parts of an individual rib and (b) its articulations.

Body part	Mass (kg)
Skull	3.94
C1-C3	0.24
C4-C7	0.38
T1-T4	0.86
T5-T8	0.83
T9-T12	0.83
L1-L3	0.83
L4-L5	0.83
Rib 2 Cartilage	0.03
Rib 3 Cartilage	0.06
Rib 4 Cartilage	0.08
Rib 5 Cartilage	0.07
Rib Lower Cartilage	0.47
Sternum	0.58
Abdomen	8

Table 1.1. Body masses. Data given by [11].

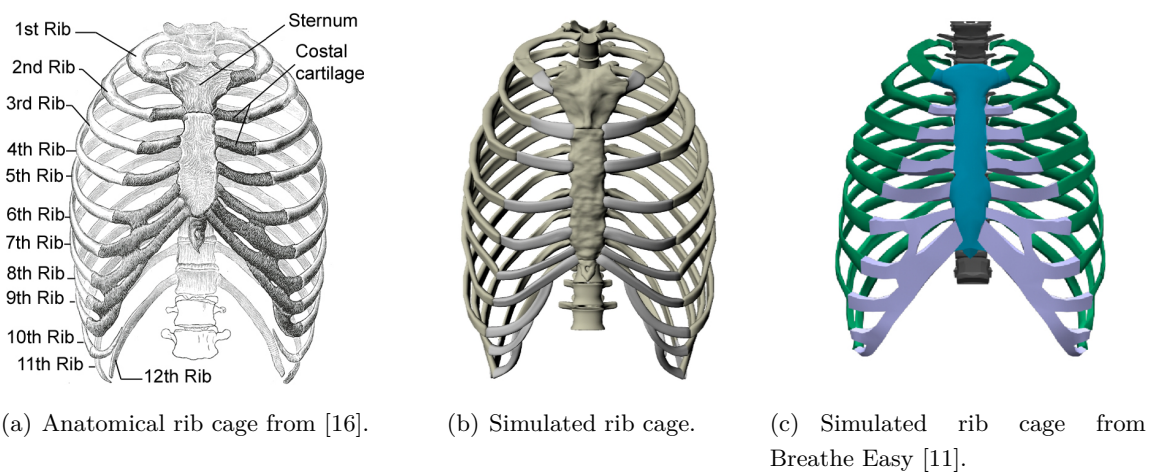


Figure 1.5. Comparison with the simulated rib cage.

2

Respiratory Muscles Simulation

As seen in chapter 1, section 1.2, breathing can be split into two different mechanisms: rib cage breathing and abdominal breathing. This chapter describes the muscle element model we used and explains in detail the muscles responsible for these two breathing mechanisms and their actions. Finally, it details how these muscles are simulated and activated in the model.

2.1. Spring muscle element

The human body is put into motion by the activation of muscles linking its different components. According to Zajac [19], there are two fundamental assumptions about real muscles:

1. A muscle can contract but not expand actively. In addition, it cannot generate force outside of its operating length range.
2. A muscle contains a damping factor which makes it resist contraction based on the speed of shortening.

Given these constraints, we modelled each muscle we used as a spring and a damper in parallel linking *nodal masses* which are in our case the different bones (this model was used and

validated by Grzeszczuk and Terzopoulos [20]). The dynamics of our biomechanical model is specified by the equations of motion (termed ‘Lagrangian equations of motion’ in [20]):

$$m_i \ddot{\mathbf{x}}_i + \gamma_i \dot{\mathbf{x}}_i + \sum_{j \in N_i} \mathbf{f}_{ij}^s = \mathbf{f}_i \quad (2.1)$$

where node i has mass m_i , position $\mathbf{x}_i(t) = [x_i(t), y_i(t), z_i(t)]$, velocity $\dot{\mathbf{x}}_i$, acceleration $\ddot{\mathbf{x}}_i$, damping factor γ_i and where \mathbf{f}_i is an external force. N_i is the set of nodes connected to node i . The spring S_{ij} , which connects node i to neighbouring nodes $j \in N_i$, exerts the force \mathbf{f}_{ij}^s on node i and $-\mathbf{f}_{ij}^s$ on node j :

$$\mathbf{f}_{ij}^s = -(c_{ij}e_{ij} + \gamma_{ij}\dot{e}_{ij}) \frac{\mathbf{r}_{ij}}{\|\mathbf{r}_{ij}\|} \quad (2.2)$$

where c_{ij} is the stiffness gain, γ_{ij} is the damping gain and $e_{ij}(t) = \|\mathbf{r}_{ij}\| - l_{ij}$ is the deformation of the spring with separation vector $\mathbf{r}_{ij}(t) = \mathbf{x}_j - \mathbf{x}_i$. The rest length of the spring is l_{ij} .

For rigid bodies (bones) in our 3D model, we use a rigid solver node to calculate dynamics and move each vertex according to the laws of physics. This node is called the *rigid solver* as detailed in [21], which solves the differential equations of the dynamics via the Runge Kutta Adaptive method, which, in comparison to the Mid-Point and Runge Kutta methods, provides greater accuracy.

2.2. Rib cage

During breathing, the rib cage is put into motion via several muscles connected to the ribs, namely the intercostals and the scalene muscles (also called the accessory inspiratory muscles).

2.2.1. Intercostal muscles

Intercostal muscles, composed of the external and the internal intercostals, are two thin muscle layers occupying the space between two ribs as shown in figure 2.1. The intercostal spaces contain two layers of intercostal muscle in their lateral portion but they contain a single layer in their ventral and dorsal portions: ventrally between the sternum and the chondrocostal junctions there are only internal intercostals called the ‘parasternal intercostal muscles’, dorsally from the angles of the ribs to the vertebrae there are only external intercostals. The external intercostal muscles have the greatest inspiratory moment in the dorsal portion of the rib cage. Experimentally, inspiratory activity in the external intercostals is highest in the dorsal area and declines gradually in the caudal and ventral directions. External intercostal muscles contract together during inspiration. Conversely, the internal intercostal muscles have the greatest inspiratory moment in the ventral area and are only active during expiration.

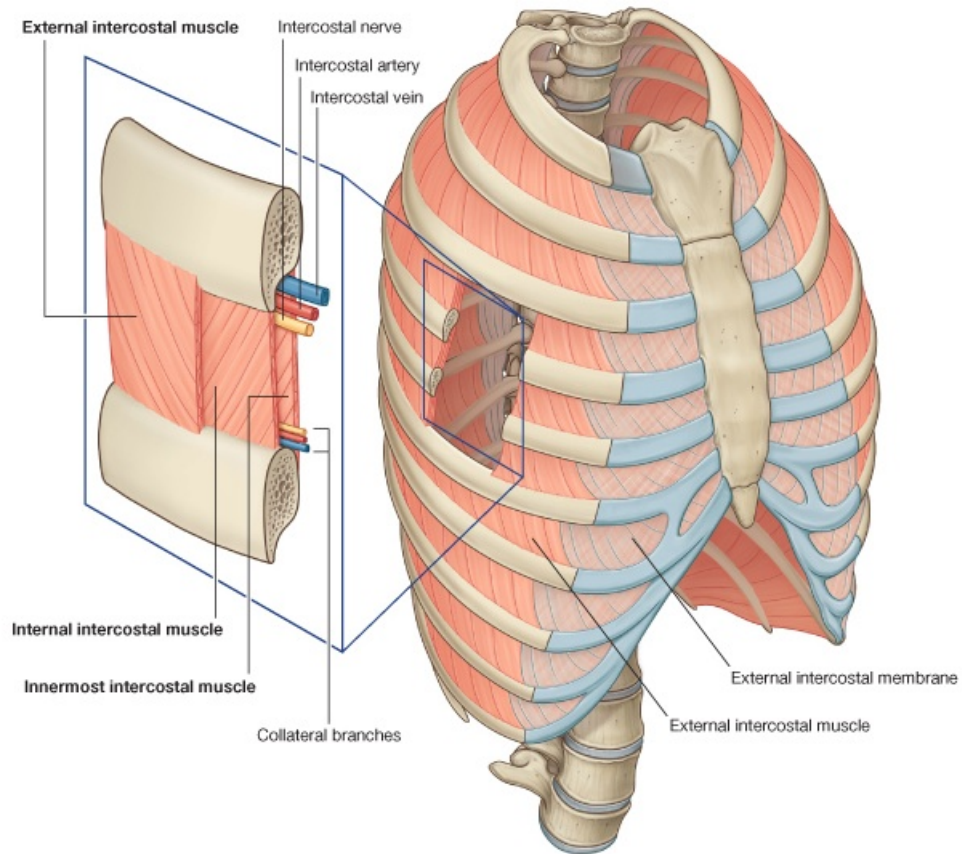


Figure 2.1. Intercostal muscles. Diagram taken from [22].

The topographic distribution of expiratory activity in these muscles mirrors the topographic distribution of expiratory effect (see figure 2.2).

We modelled the internal and external intercostal muscles with spring muscle elements as described in section 2.1. Between each rib, twelve to fourteen spring elements were attached to simulate the intercostal muscles. To model each intercostal layer, 250 spring muscle elements were used (see figure 2.3).

2.2.2. Scalene muscles

The scalene muscles comprise three muscle heads that run from the transverse processes of the lower five cervical vertebrae to the upper surfaces of the first two ribs as shown in figure 2.4(a). When activated, the scalene muscles produce an expansion of the upper rib cage. Although they have been considered to be ‘accessory’ muscles of inspiration, electromyographic studies have established that they invariably contract during inspiration.

We modelled the scalene muscles with 12 spring elements linking the cervical vertebrae C6 to the first rib as shown in 2.4(b).

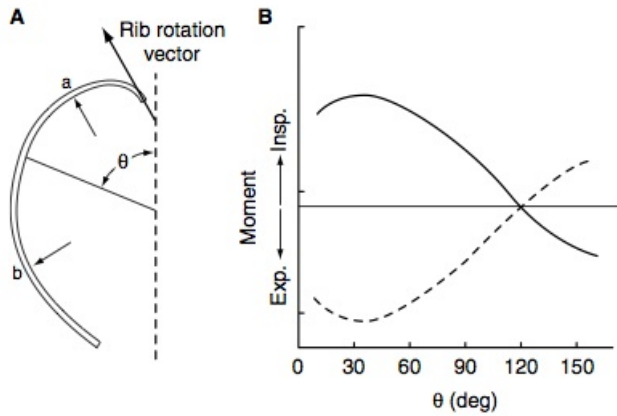
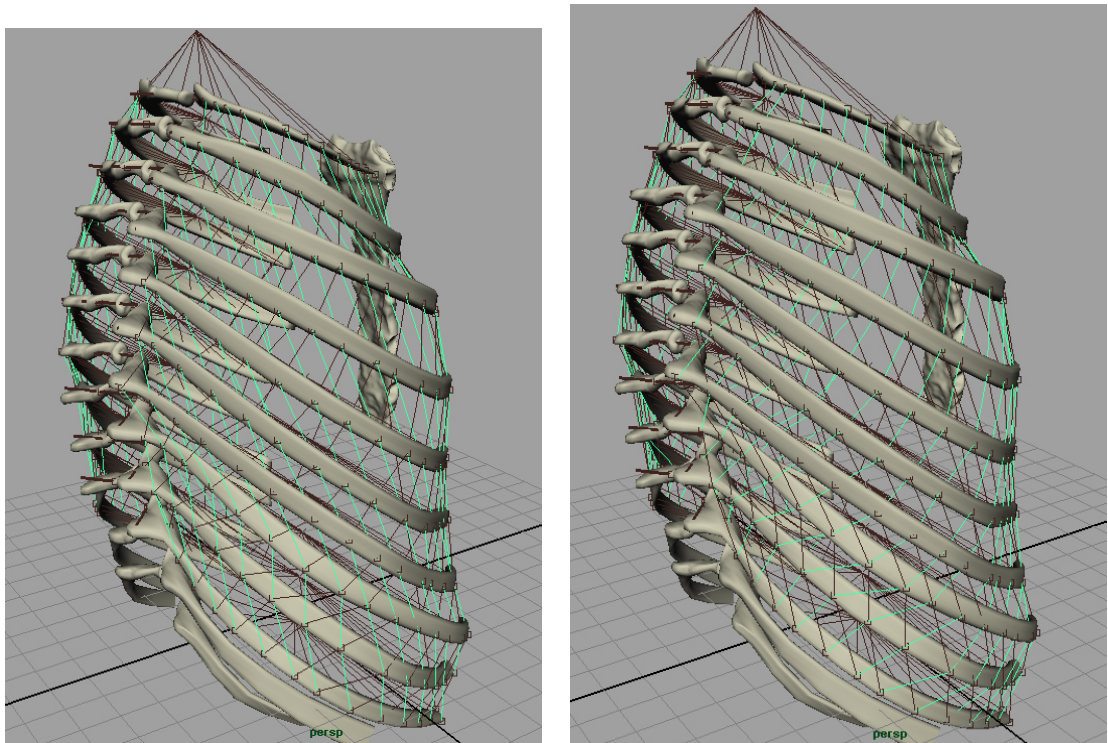


Figure 2.2. Effects of rib curvature (B) on the net moment exerted by an intercostal muscle located by the angle Θ (A). The external intercostal muscle (continuous line) has the greatest inspiratory moment in the dorsal portion of the rib cage (Θ between 15° and 60°), this moment decreases and reverses into an expiratory moment for $\Theta \geq 120^\circ$. The internal intercostal muscle moment (dashed line) mirrors the external intercostals. In this case and for the rest of this report, the verb to mirror is employed in the sense to reverse around the mean. Diagram taken from [23].



(a) When activated, the external intercostal muscles, in green, lift up the rib cage.
 (b) When activated, the internal intercostal muscles, in green, move the rib cage down.

Figure 2.3. (a) simulation of the external intercostal muscles and (b) the internal intercostal muscles.

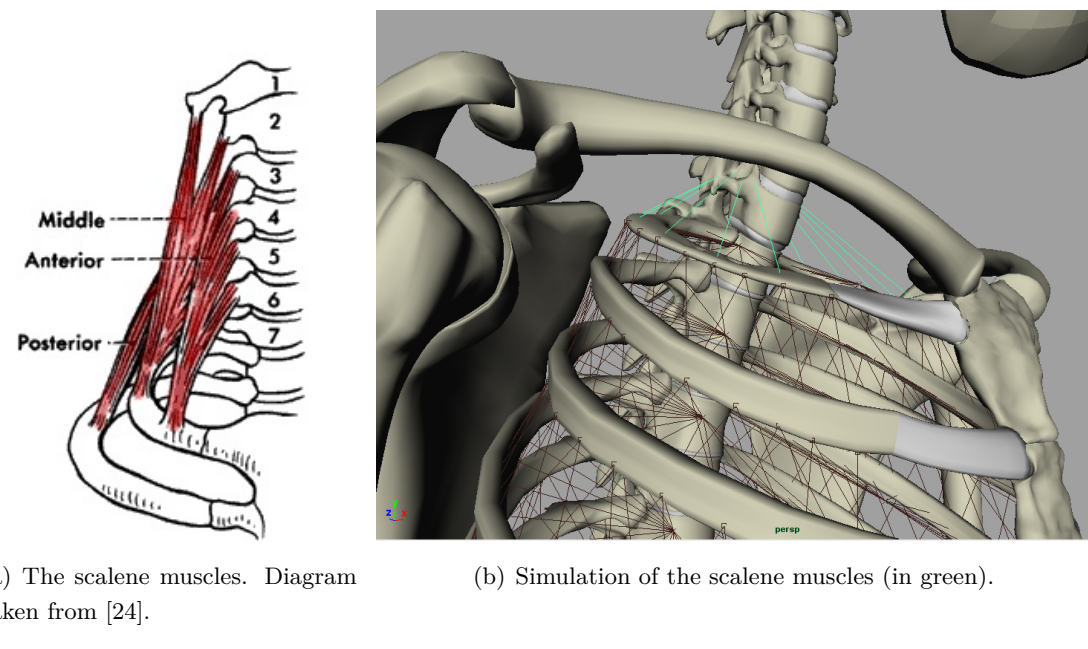


Figure 2.4. Comparison with the simulated scalene muscles.

2.3. Abdominal cavity

The abdominal cavity is the cavity of the human body that holds the bulk of the viscera. It is located inferior to the thoracic cavity, and above the pelvic cavity. Organs of the abdominal cavity include the stomach, liver, gallbladder, spleen, pancreas, small intestine, kidneys, and large intestine. The abdominal compartment contains between 100 and 300 mL of abdominal gas and the rest is incompressible. Therefore it can be reasonably considered as fully incompressible: any local inward displacement results in an equal outward displacement elsewhere in the compartment. Furthermore, the abdominal compartment is fixed dorsally to the spine, caudally to the pelvis and laterally with the iliac crests; which constrains the area of the abdominal compartment that can be displaced to the ventral abdominal wall and the diaphragm. The diaphragm itself is made of muscle fibres which insert onto the lower six ribs. During inspiration, when the diaphragm contracts the muscle fibres of the diaphragm shorten, and as a result the dome of the diaphragm goes down and the ventral abdominal wall moves outwards. This process expands the thoracic cavity along its cranio-caudal axis and displaces the abdominal viscera pushing the ventral abdominal wall outwards. As the diaphragm is connected to the lower six ribs, its contractions apply a force (called the insertional force) on these ribs in the cranial direction, lifting the ribs and rotating them outward such that the lower rib cage expands. Conversely, during relaxation when the abdominal muscles contract, the ventral abdominal wall moves inward and as a consequence, the diaphragm has a cranial motion up into the thoracic cavity. The mechanism is illustrated in figure 2.5. The diaphragm can shorten by 30 to 40 % according to the authors of [23]. From an anatomical point of view, there are four abdominal muscles: the rectus abdominis muscle (the most ventral, it runs caudally along the whole length of the abdominal wall), the transversus abdominis (the deepest of the muscles

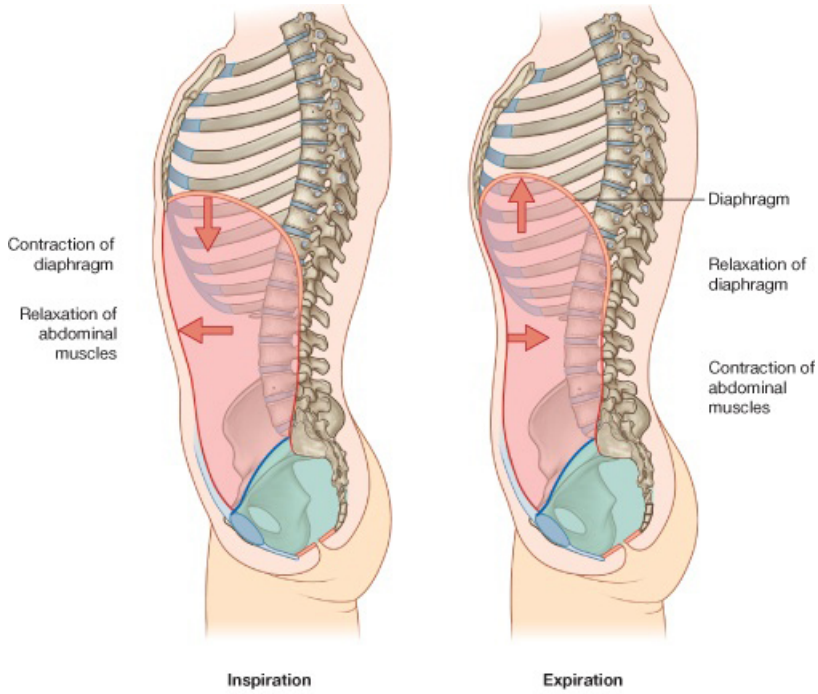


Figure 2.5. Sketch of how the abdomen assists in breathing. Diagram taken from [22].

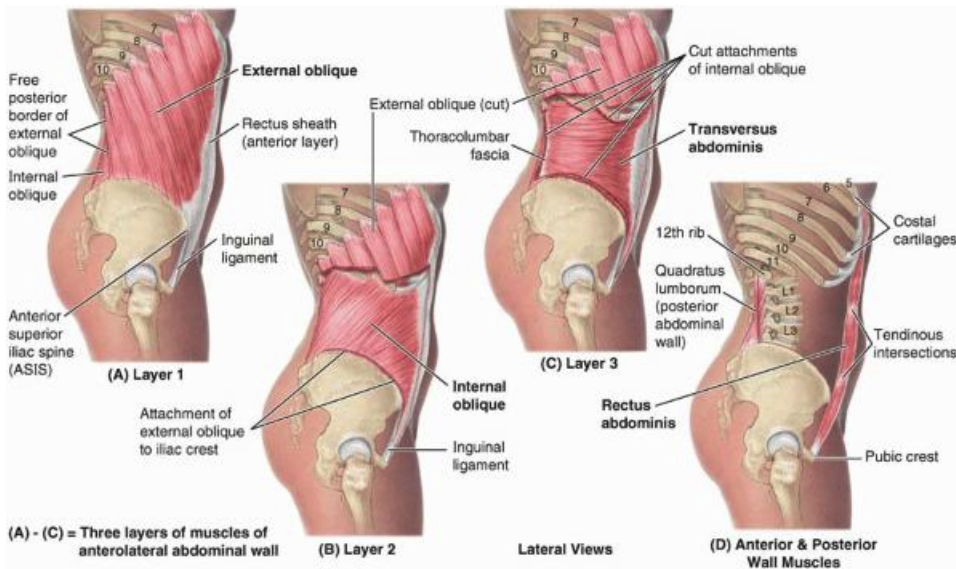


Figure 2.6. The abdominal muscles. Diagram taken from [18].

of the lateral abdominal wall), the external oblique muscle (the most superficial, it contracts caudally and medially) and the internal oblique muscle (see figure 2.6).

Posture also has an effect on breathing. For instance a change from the seated to the supine position increases the abdominal compliance, so the resistance from the abdominal contents to diaphragmatic descent is less effective and the forces applied by the diaphragm to expand the lower rib cage are reduced.

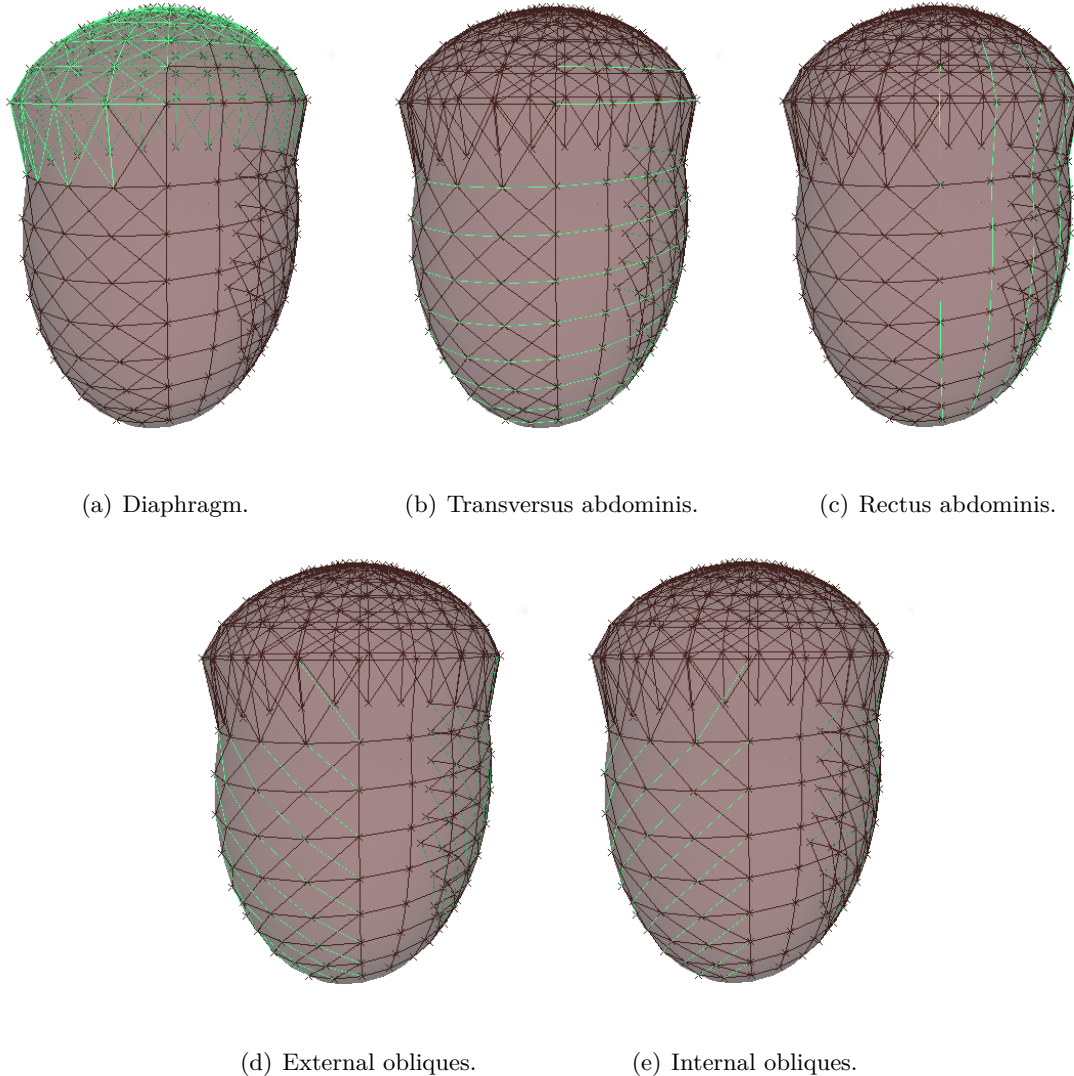


Figure 2.7. *Simulation of the different muscles of the abdominal cavity involved in breathing.*

We modelled the abdominal cavity by deformation of a polygonal sphere to produce the shape of the belly (see figure 2.8). Then, we added the different muscle elements by attaching each muscle end to a vertex on the surface of the simulated cavity. The diaphragm was modelled with 500 spring muscles located at the top of the abdominal cavity (see figure 2.7(a)). The four abdominal muscles were also modelled with spring muscles and 100 of them were used for the transversus abdominis (see figure 2.7(b)), 50 for the rectus abdominis (see figure 2.7(c)), 60 for the external obliques (see figure 2.7(d)) and 60 for the internal obliques (see figure 2.7(e)).

2.4. Control of the model

The nature of the activation functions of the muscles involved in breathing are not currently well-defined, in either the medical or the animation communities. Nevertheless, some research

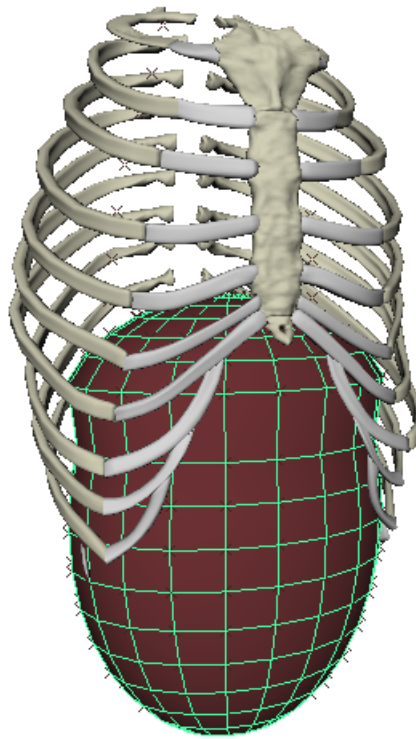


Figure 2.8. Simulation of the abdominal cavity.

is available in the literature and previous modelling attempts provide useful information concerning these activation functions.

As we are using spring muscle elements, we control the activation of each muscle by changing the contraction value as a time varying input parameter. Steady-state breathing is ideally periodic (usually 13–17 breaths per min in the average human [25]); for that reason we naturally sought periodic input activations. Two major kinds of input have previously been proposed to control animation of physical muscle simulations: hand-crafted curves as Chen et al. [26] used in their model or sine functions as used by Terzopoulos et al. [27] and the Breathe Easy model [11]. In the latter, the authors experimented with both smooth and abrupt changes for the periodic contraction using simple sinusoid and step functions and concluded that sine functions created the desired response in steady-state breathing. As a consequence, we have also used different sine functions to stimulate the different muscles during steady state breathing.

Concerning the contraction of these muscles, Klute et al. [28] found a contraction range from 0.7 to 1.2 for their artificial muscles. We used these data as limit constraints for our input functions.

The damping and stiffness parameters of the spring muscle elements as described in equation 2.2, were set to 1 for the intercostal and diaphragm muscles in order to have a system as close as possible to a *critically damped* system (a system that converges to zero faster than any other without oscillations). These parameters were found empirically to avoid undesirable

oscillations when the spring muscle elements were activated.

We activate a spring muscle element by changing its length $l(t)$ in time. For steady-state breathing, this length is modulated by a general sine function $r(t)$ in our simulation:

$$l(t) = l_0 \times r(t) \quad (2.3)$$

$$r(t) = \alpha - \frac{\beta}{2} (\sin(2\pi f_b t + \phi) + 1) \quad (2.4)$$

where:

- l_0 is the rest length of the spring muscle element,
- $\alpha \in [1, 1.2]$ is the offset value (i.e. the upper limit of function $r(t)$),
- $\beta \in [0, 0.5]$ is the contraction value,
- f_b is the breath frequency,
- ϕ is the phase.

The rest of this chapter describes the different activations we used for the muscles involved in chest and abdominal steady-state breathing.

2.4.1. Chest breathing

In chest breathing, three groups of muscles are active: the external intercostals, the internal intercostals and the scalene muscles. In contrast to other recent simulations [11, 7, 12], we did not apply the same activation inputs for all the intercostal muscles. As shown in 2.2.1, the external intercostal muscles have an inspiratory moment which is the highest in the dorsal portion of the rib cage and decreases and reverses into an expiratory moment in the front of the rib cage and the internal intercostal muscles' moment mirrors that of the external intercostals (they have their highest expiratory moment in the front of the rib cage that decreases gradually along the rib in the dorsal direction to finally reverse to an inspiratory moment in the back part of the rib cage). For this reason, the activation functions in the external intercostal muscles were tuned such that the contraction value decreases along the rib from the head to the junction with the cartilage of the rib. The activation functions of the internal intercostals mirror the external ones.

The scalene muscles, located in the neck were grouped together.

Figure 2.9 shows the different activation functions $r(t)$ of the intercostals and the scalene muscles for one visually plausible breathing situation.

2.4.2. Abdominal breathing

We modelled the abdominal cavity as one incompressible volume as justified in section 2.3. During inspiration, the diaphragm (at the top of the abdominal cavity) contracts pushing the front of the belly outwards. During expiration, the diaphragm relaxes and goes up to its rest state, the abdominal muscles contribute in pushing the front of the belly inwards—even if they are not necessarily contracting. From a modelling perspective, the vertices of the polygonal sphere used to simulate the abdominal cavity are passive at the bottom and the back side, while those on the diaphragm, the lateral and front parts are active. To model the movement given the incompressibility constraint, we used a pressure approach as in [11]. We assume that the pressure P inside the cavity is determined by Hooke's law:

$$P \propto \left(\frac{V_0}{V} - 1 \right) \quad (2.5)$$

where V_0 is the original volume and V the current volume of the abdominal cavity. The coefficient of proportionality is called the ‘bulk volumetric modulus’ and controls the substance’s resistance to uniform compression. We found 0.3 Pa to be satisfactory. Since in our model the surface of the cavity is polygonal, being composed of triangles, the volume is calculated as the sum of tetrahedra (the base of each tetrahedron is a triangle of the surface and the apex a fixed point inside the polyhedron) inside the cavity. In order to make the active vertices of the front of the belly move outwards when the diaphragm contracts, for each active vertex, a force \mathbf{F}_v proportional to the pressure P times the area A of the triangle attached to the vertex (this is defined by a specific ordering) is applied:

$$\mathbf{F}_v = P \times \frac{A}{3} \mathbf{n} \quad (2.6)$$

where \mathbf{n} is the direction vector of the force perpendicular to the triangle. The division by 3 accounts for the three vertices composing the triangle.

The abdominal muscles (see figure 2.6) can work autonomously, trying to preserve the pressure in the abdominal cavity by contracting to their rest lengths when they are stretched. However, they can also be activated to help the front of the belly move inwards more rapidly (some people and particularly sportsmen, actively use these muscles during expiration).

In the steady-breathing case, the diaphragm moves periodically and for that reason, we activate it with a sine function described in section 2.4. An example of such an activation function for the diaphragm can be seen in figure 2.9.

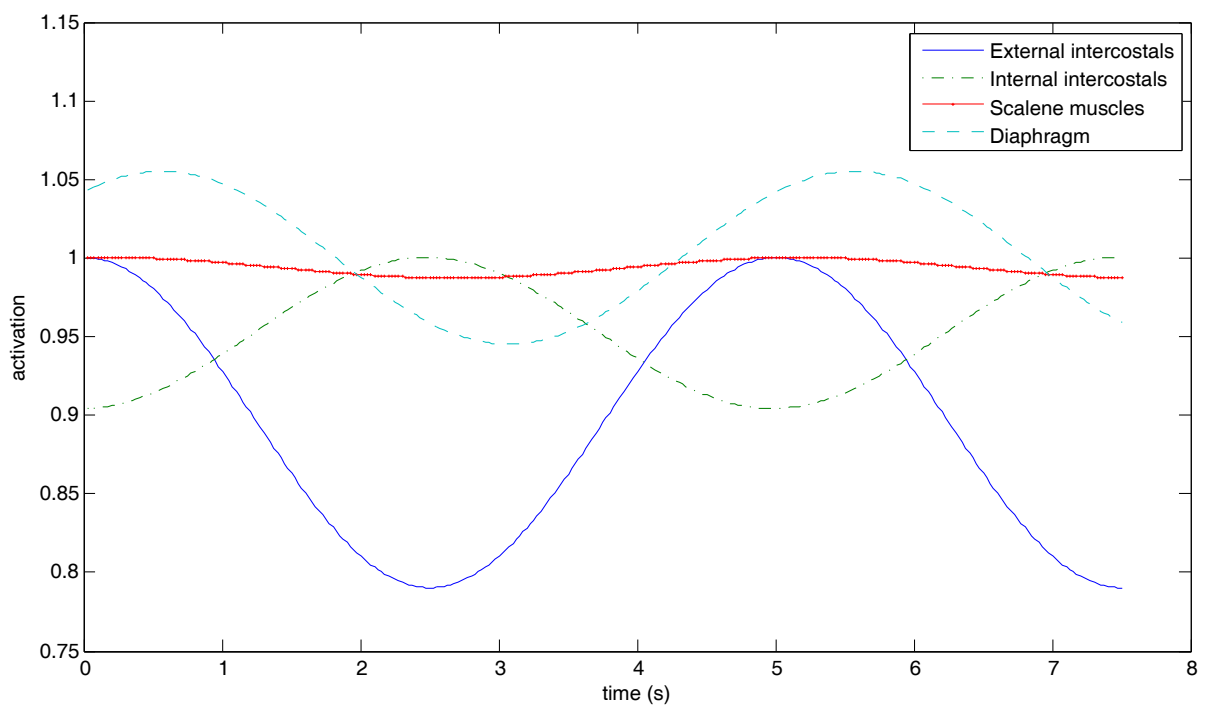


Figure 2.9. Activation functions of the different muscles for a plausible simulation.

3

Fitting Datasets to the Model

Recall that the main goal of this work is to investigate pulmonary function of a patient using the Structured Light Plethysmography technique. Now that we have at our disposal a simulation of the human torso with high level controls, we present a data-driven approach to drive the model. For this purpose, we need to adapt the simulation to both the patient’s anatomy (by fitting an appropriate skin mesh) and the patient’s breathing (by deriving the control parameters from the SLP dataset). To date, only [11] has proposed a data-driven approach to model the behaviour of actuated physically-based deformable muscles. However, the constraints and hypotheses they use are questionable and will be discussed further in section 3.4. In addition, there appears to be no previous work related to the fitting of a skin mesh to a particular anatomy in breathing applications.

In section 3.1, we will briefly present the SLP technique and the nature of the data it provides. Section 3.2 will explain how we fit an adapted skin mesh to the model and section 3.3 will describe how this skin mesh is deformed according to the rib cage and abdomen motion. Finally, section 3.4 details the optimisation algorithms used to fit the SLP dataset to the model.

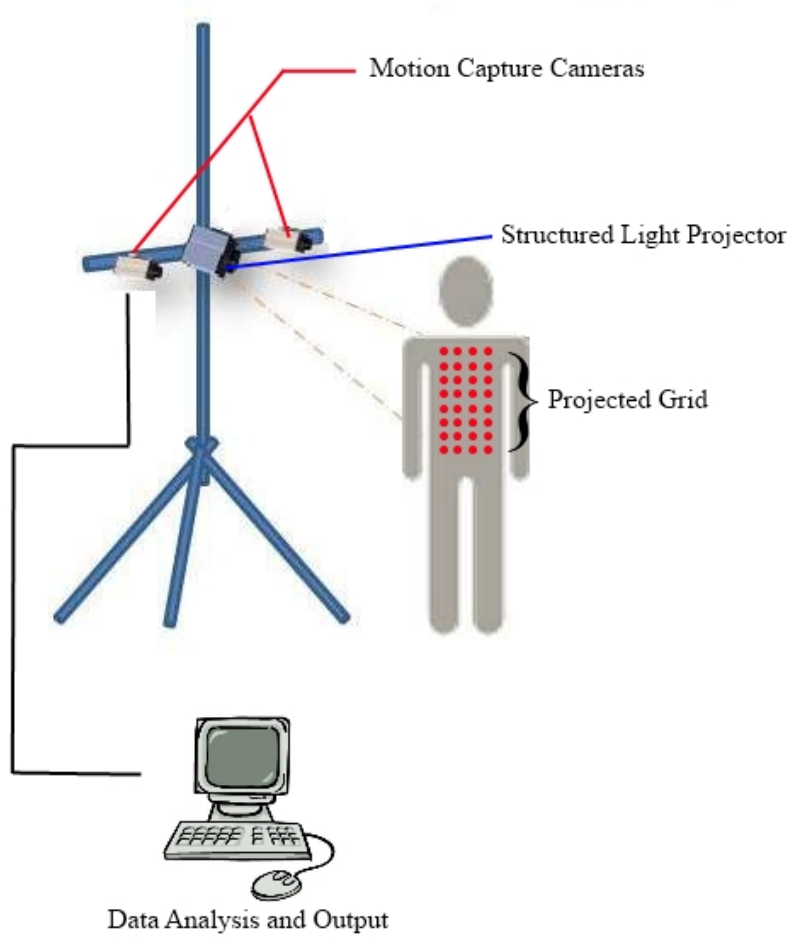


Figure 3.1. Diagram of the Structured Light Plethysmography device.

3.1. Structured Light Plethysmography datasets

Structured Light Plethysmography is a non-invasive method for pulmonary function testing using visible light [2]. This technique uses two motion capture cameras and a known grid which is projected onto the chest and abdomen of a patient as figure 3.1 illustrates.

It relies on triangulation to reconstruct the space locations of the grid points projected by combining the images of the two cameras for each frame (see figure 3.2). Once the grid points are tracked, put into correspondence and reconstructed, only those on the chest and abdomen areas are retained—this is done by a heuristic procedure [29]. More details can be found concerning the reconstruction step in the SLP technique in [30].

The SLP system ultimately provides us with the space coordinates over time of the grid points that are located on the chest and abdomen of a patient breathing. From the 25x30-point initial grid, a subset of varying size usually from 5x5 to 10x10 is finally retained.

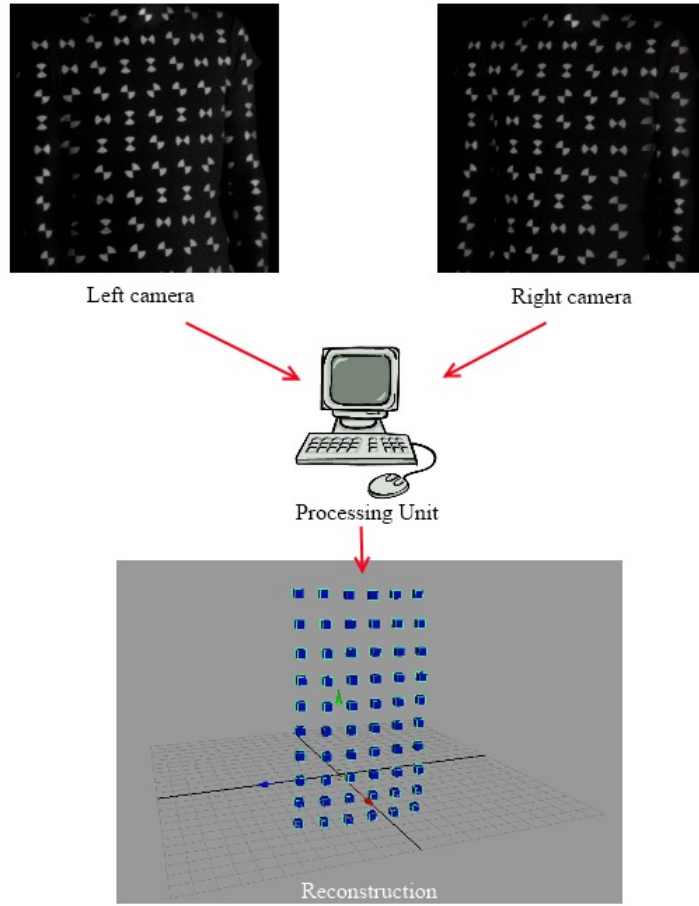


Figure 3.2. SLP in action: the images from the left and right cameras are processed to track the grid points which are then put into correspondence and reconstructed.

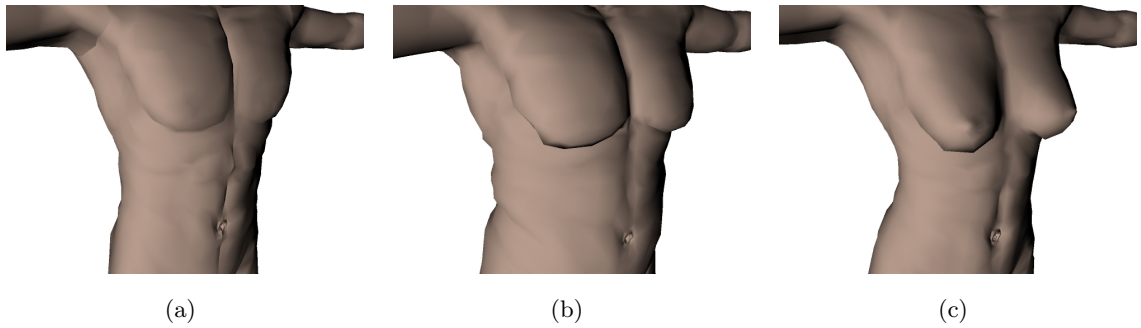


Figure 3.3. Personalised skin meshes derived from Make Human [31] according to physiognomy data. (a) male, 22-year old, 1.75 m, 68 kg, 0 % breast size. (b) male, 40-year old, 1.70 m, 80 kg, 0 % breast size. (c) female, 30-year old, 1.65 m, 55 kg, 80 % breast size.

3.2. Adapting a skin mesh

In this section we will use a number of 3D computer graphics terms:

rigging: the process of creating the bone structure (also called the skeleton) for a character.

skinning: the process of binding a skeleton to a single mesh object.

skinning deformation: the process of deforming the mesh as the skeleton is animated or moved.

In our case, the skeleton is composed of bones (ribs, vertebrae, sternum), a deformable part (the abdomen) and joints linking the bones to each other. Our goal is to fit an adapted skin mesh to this skeleton and deform it as the skeleton moves.

To have a simulation as close as possible to a patient's anatomy, it is crucial to have a skin mesh which closely matches the patient's external shape. In addition, as the SLP only captures the front of the chest wall, the skin mesh and the skinning deformation have to be done with special care, otherwise significant fitting errors would be introduced in the optimisation step.

To help understand the different steps of adapting a skin mesh to a patient, we will use the following real life example for the rest of this section: a subject is asked to breath in different positions in front of an SLP device. The grid is projected so that the first row is aligned with the line defined by the clavicles of the subject; this procedure allows us to have spatial reference points to later place the grid onto the model's skin. The subject is asked to wear a tight T-shirt to avoid skin features and creases which might distort the grid projected by the SLP device. We usually end up with a 6x10 grid over 1000 frames corresponding to about 16.7 seconds and 4 breaths.

From the coordinate matrices the SLP system outputs for the grid points on each frame, we match each grid point of the SLP system to a box marker in the simulation (see figure 3.2). Each marker moves according to the space location of the grid point it is matched to. The first step consists of scaling the model to the SLP scale, or conversely, converting the space coordinates of the SLP reconstructed grid points to the scale of the model. This is trivially done by computing a known distance (for instance between two grid points) on the model and comparing it to the actual distance given by SLP.

From physiognomy data of the patient (gender, age, height, weight, breast size) we derive a skin mesh using the Make Human [31] software (see figure 3.3), which is an open source tool for making 3D characters. The skin obtained is generally a good initial fit to the patient's torso as the skin is high resolution (6572 vertices and 19683 edges in total) and the physiognomy parameters sufficiently definite, for a good level of personalisation. The next step is to correctly position the SLP grid onto the skin mesh. The grid is manually placed onto the skin (figure 3.4(a)) by applying a global rotation and translation matrix to all the grid point coordinates. This is done by aligning the points of the first row of the SLP grid (originally projected on the line defined by the clavicles during the experiments) to the clavicle's line on the skin mesh. We then derive the transformation matrix that we then apply to all grid points. The frame used to initialise the position of the grid on the skin has to correspond to the inflexion point of breathing between expiration and inspiration (when the expansion of the rib cage and the

abdominal cavity are minimum). In our example, this frame is conveniently at frame 1.

We compute the error between the skin mesh and the current SLP grid by summing the distances between each grid point and the closest vertex on the skin, this value is then normalised by dividing it with the number of grid points to finally obtain the skin fitting error. In our example, the initial error between the skin and the grid points is 0.5091 cm (see figure 3.4(d)). However, we will now see that this mesh skin can be improved and fitted more precisely to the patient’s anatomy.

Even though the skin mesh is composed of many vertices, the distance between a grid point and its associated vertex is still significant—given that we have a mean error of 0.5091 cm and that the actual breathing displacement of the rib cage can be lower than 0.5 cm in the medial direction. Moreover, some points contribute much more in the error function than others (the variance is 0.0329 cm², see figure 3.4(d)). To lower the error of the skin fitting, our approach was to displace the vertices to the grid point locations they are associated with (see figure 3.4(b)) and then to smooth the whole skin to avoid skinning artefacts; this is done for each dataset even for the same patient (from one experiment to another, there may be movements of the patient that lead to creases of the T-shirt worn and as a consequence to skinning artefacts). The smoothing is done by averaging the values of the five closest vertices for each vertex of the skin mesh (see figure 3.4(c)) producing a smoother surface without modifying the topology of the skin. We finally find a much better fit, with a mean skin fitting error of 0.1404 cm and a variance of 0.0038 cm² (see figure 3.4(e)).

3.3. Skinning deformation

Once the skin mesh fits the patient’s anatomy, it has to deform according to the animation of the underlying skeleton. In most situations, when it comes to skinning deformation problems, the skeleton structure is simpler and made of joints linked with wires referred to as *bones*, this is the so-called rigging process. In our case, the skeleton is more complex as the moving parts of our model are the sternum, the ribs and the abdominal cavity.

The *de facto* standard in real-time algorithms for mesh deformation makes use of a set of per-bone weights associated with each vertex of the skin mesh. Each vertex has a per-bone weight giving a measure in the range [0, 1] of the influence of the particular bone on that vertex. These weights are normalised so that the sum of all per-bone weights for a particular vertex is 1. Traditionally the task of assigning the weights has been done manually and consisted of going through all bones of the skeleton and carefully adjusting the weights with a ‘weight painting brush’ onto the skin mesh. Baran and Popović [32] developed a method, namely *bone heat*, that can automatically derive the skin weights. This technique models weight assignment as a heat diffusion system on the surface of the mesh. For each bone, the vertices which have that bone as their nearest visible bone are initialised to have a surface temperature inversely proportional to the square of their closest distance to the bone. Wareham and Lasenby [33]

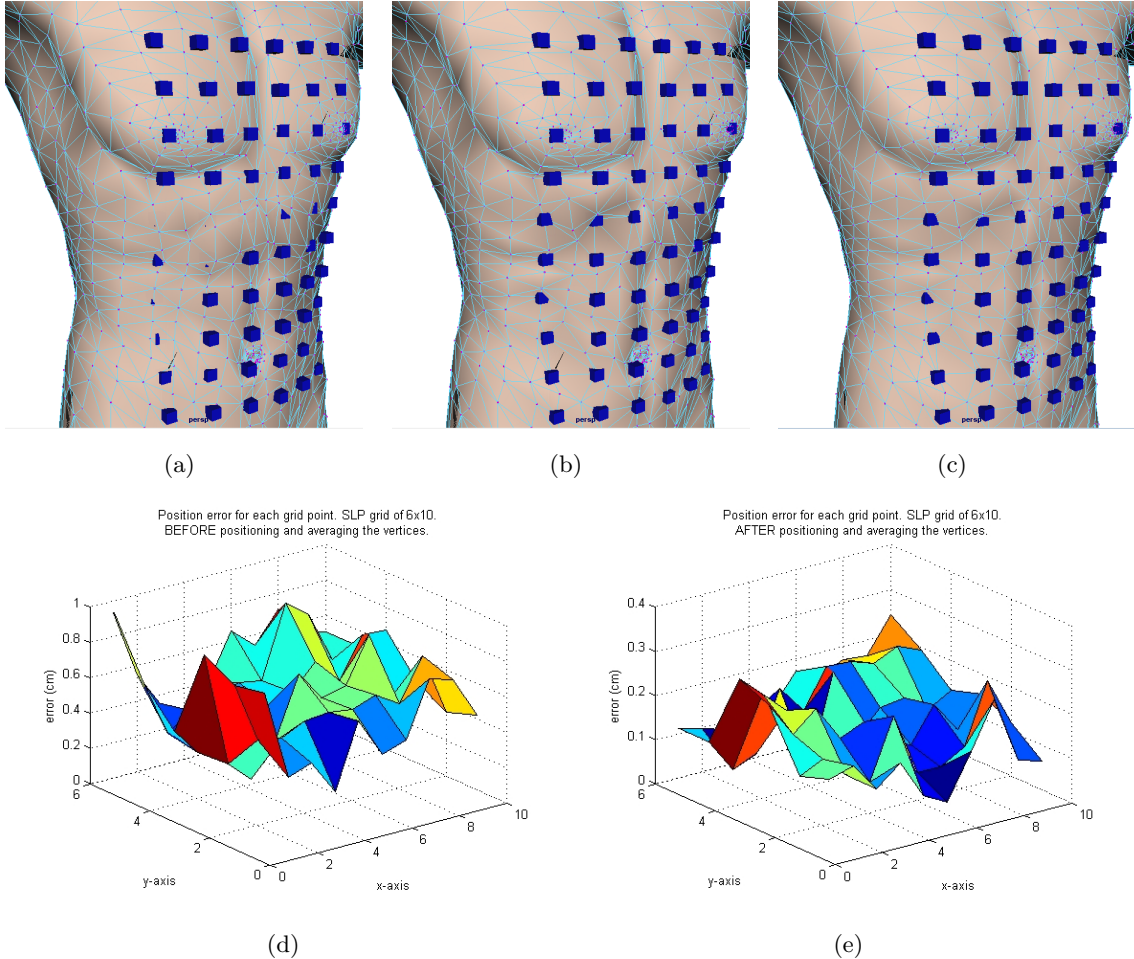


Figure 3.4. The process of fitting a skin mesh. (a) the SLP grid points are subjected to a global geometric transformation in order to locate them on the initial skin mesh. The frame chosen to initialise the grid corresponds to the inflexion point between inspiration and expiration of the patient. In our example it corresponds to frame 1. (b) each vertex associated with a grid point is moved to the grid point location. (c) the skin mesh is then smoothed by averaging each vertex location with its immediate neighbours. (d) the error (z-axis) is plotted for each point of the 6x10-point grid (x-axis and y-axis) with the initial skin mesh at frame 1. The mean error is 0.5091 cm and the variance 0.0329 cm². (e) the error (z-axis) is plotted for each point of the 6x10-point grid (x-axis and y-axis) with the new skin mesh (after the vertices were re-positioned and averaged) at frame 1. The mean error is 0.1404 cm and the variance 0.0038 cm².

propose a refinement of *bone heat*, termed *bone glow*, which copes with *bone heat* weaknesses when it comes to assigning weights on surfaces containing creases. However, as the deformation of the skin implied in breathing does not involve any twisting, creases or any distortion of that type on the skin, we use *bone heat* (available in Maya 2010) for the automatic weight assignment algorithm; the final map representing the weights over the skin mesh in our example can be seen in figure 3.5.

Once the weights for each vertex are assigned, several techniques can be used to deform the skin mesh; the most commonly used is the Linear Blend Skinning (LBS) [34]. LBS consists

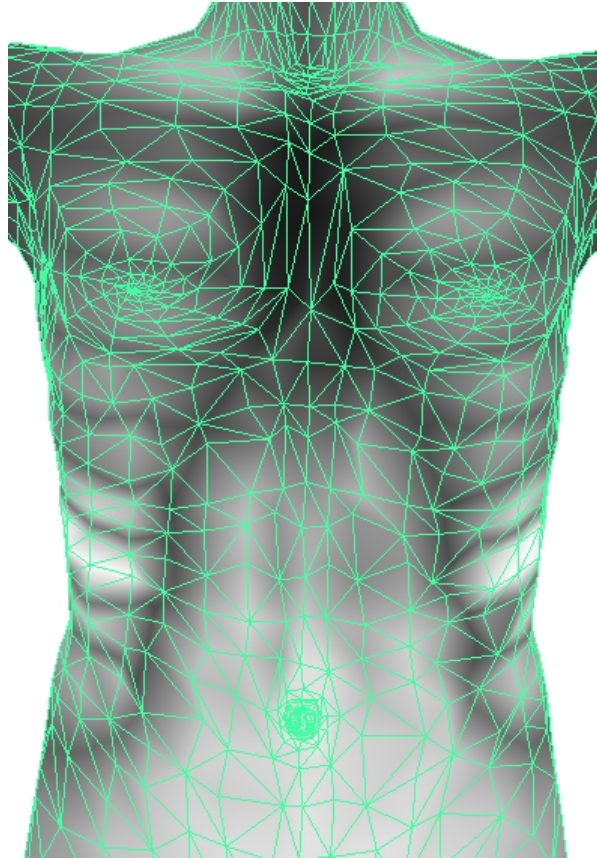


Figure 3.5. Skin weights of the fitted skin mesh. Each vertex of the skin is assigned weights that correspond to the influence of the different underlying bones. The sum of the weights assigned to each vertex, defining the influence of the underlying bones onto the skin mesh, has been indicated using a gradation from black to white to represent the range [0, 1].

in deforming vertices as a weighted linear combination of the movement of the bones they are attached to. Some improvements to this algorithm have been designed to cope with artefacts that may appear around joints that are bent or twisted too far. Mohr and Gleicher [35] add rotations and scale joints to the skeleton, Kavan et al. [36] use spherical and dual-quaternion interpolation schemes. However, as the movements in breathing don't involve creases, bends or twists of the skin, the LBS method seemed the most relevant method to apply in our case in terms of computing efficiency and quality of the skinning deformation.

Consequently, at this stage, we have a simulation of the human torso with a skin mesh fitted to a patient's anatomy. This skin mesh is deformed according to the underlying skeleton motion which is driven by the activations of the respiratory muscles.

3.4. Fitting of SLP datasets

The final phase for generating an animation is the integration of the breath motion data from SLP to our torso simulation. To this end, we explore adaptation methods that employ op-

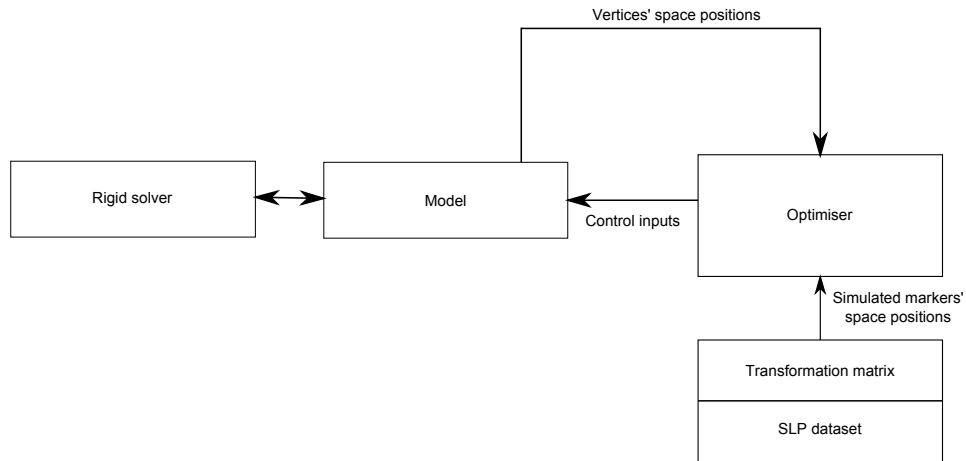


Figure 3.6. *SLP-driven system overview.*

timisation techniques to modify a generic model of respiration to fit the breathing patterns and characteristics of specific individuals. Because the datasets given by SLP cannot be directly used to control the simulation, the optimisation attempts to derive the different muscle activations of our simulation to fit a given SLP dataset.

The SLP-driven system overview can be seen in figure 3.6.

The SLP dataset is fed into the optimiser to determine the best control inputs to feed into the torso simulation. This generates movement from the model that is used to compare to the SLP dataset. The optimiser, iteratively updates the parameters of the control inputs so as to minimise the discrete cost function to produce increasingly better fits of the dataset. We set the cost function to be the error between the human and simulated motion data as:

$$f_{error} = \frac{\sum_{i=1}^f \sum_{j=1}^p d(i, j)}{f \times p} \quad (3.1)$$

where f is the number of frames, p the number of SLP grid points and $d(i, j)$ the distance between the j -th SLP grid point and its associated vertex on the skin mesh at frame i .

At each step, the optimiser computes the cost function and infers the next set of input parameters. The cost function is derived from the SLP grid point locations (after being geometrically corrected for projection effects through the application of a transformation matrix), and the space positions of the vertices associated with each grid point. The positions of these vertices are computed by the dynamic solver which takes into account the control inputs given by the optimiser and the model.

As the cost function determination requires a lot of computing power (between 20 and 30 minutes on an Intel(R) Core(TM) i5 CPU for a sequence of 1000 frames), we would like the optimisation algorithm to converge in a small number of iterations. One direct way to achieve

this, is to keep the number of parameters to be optimised over reasonably low. The controllers we chose are derived from standard activation sets (see figure 2.9): one for the activation level of the rib cage muscles (the external and internal intercostals and the scalene muscles), another for the diaphragm activation level and a last one for the phase shift of the whole sequence. The breath cycle is derived beforehand by analysing the characteristics of the SLP motion data.

We use the Simplex Down-Hill method designed by Nelder and Mead [37] to optimise the cost function. For all our simulations, the algorithm converges in less than 60 evaluations of the cost function and we end up with a cost error in the range of [0.1, 0.5] cm.

Table 3.1 shows the results of the optimisation process with the same subject breathing in different positions (standing, sitting and lying) and figure 3.7 gives the derived volume curves of the lungs for the different positions.

position	A_{ribs}	$A_{diaphragm}$	iterations	f_{error} (cm)
standing	48	50	52	0.2736
sitting	17	57	33	0.3727
lying	55	62	51	0.3813

Table 3.1. Control parameters derived from the same subject breathing in different positions. A_{ribs} and $A_{diaphragm}$ correspond to the activation percentage of the maximum reachable activations of the ribs muscles and the diaphragm respectively.

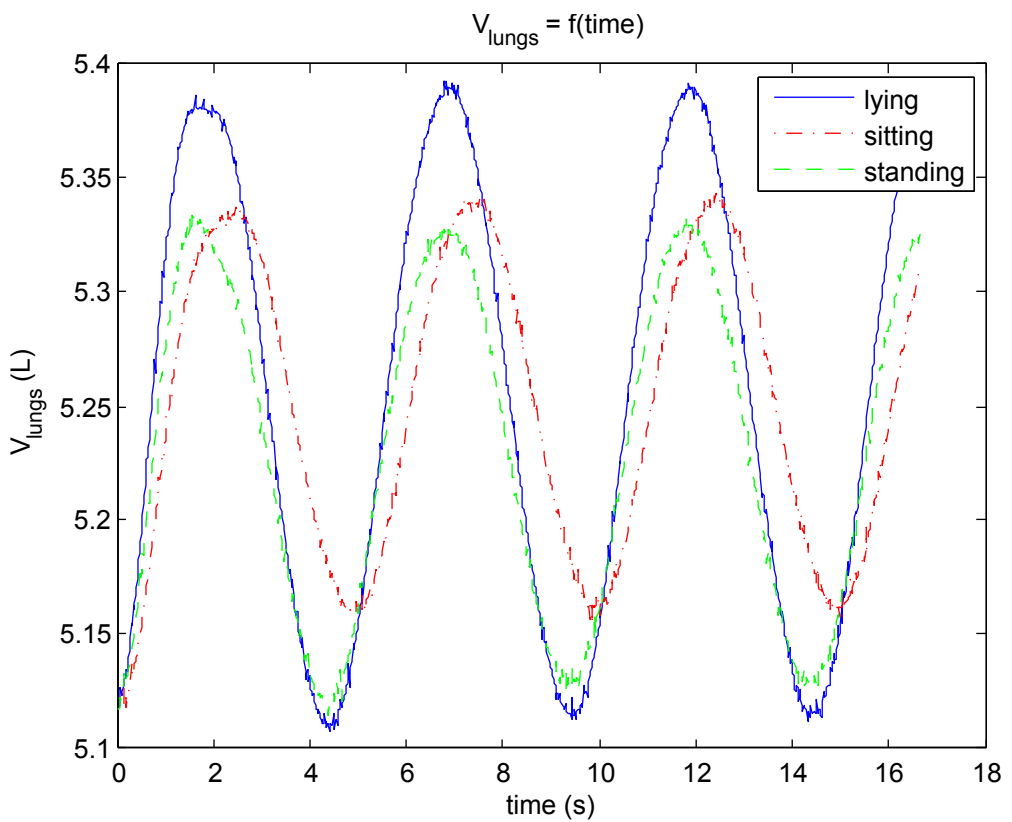


Figure 3.7. Volume of the lungs derived from the simulation of the same subject breathing in different positions.

4

Validation of the Simulation

In order to validate our model, we had to compare the results obtained with our technique to another medically verified one. We chose the spirometer which is both the most widely used device and the *de facto* standard pulmonary function testing device used by lung specialists. This chapter explains the technique used to test the validity of our method. Firstly, it describes the protocol followed to acquire data and provides an analysis of the data obtained on three subjects. Secondly, it states the different comparison techniques and the results achieved with our datasets.

4.1. Experiment set up

A laptop-based CardinalHealth UK MasterScope spirometer from Addenbrooke's hospital, Cambridge was kindly lent by Dr. Richard Iles, Consultant in Respiratory & General Paediatrics, who is also involved in the SLP project. This system was chosen as it incorporates the widely used Fleish screen pneumotach. In addition, the derived flow signal can be exported in a machine-readable format using the manufacturers' software, JScope 32.

There are different techniques that can be used to design a spirometer; the one we used belongs

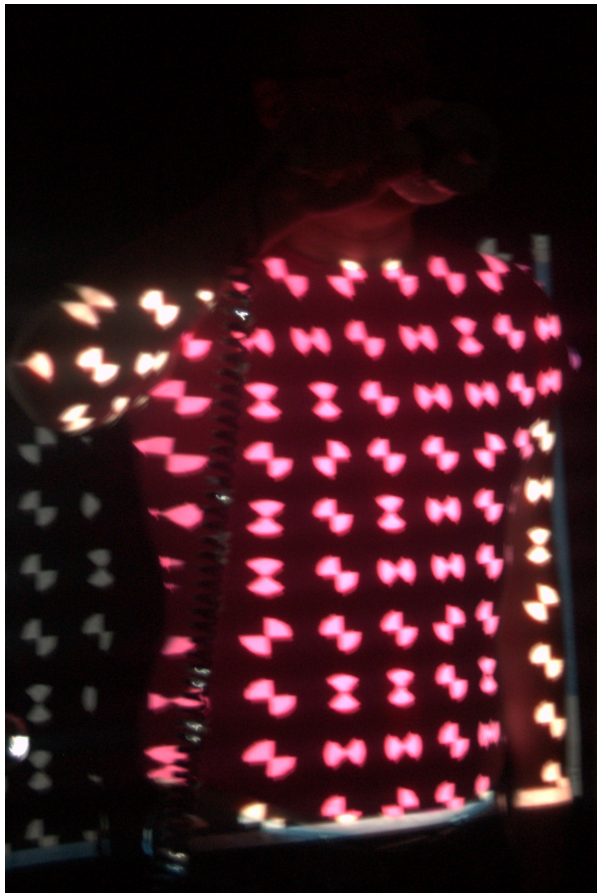


Figure 4.1. Experiment set up: both the SLP cameras and the spirometer are recording.

to a specific type of spirometers called *pneumotachometers*. A pneumotachometer measures the flow rate of gases by detecting pressure differences from a tube inserted in the mouth of the patient which is then processed to eventually give the volume flow over time. The pneumotachometer we used requires input of some of the patient's anatomy characteristics: gender, age, weight, height and the room conditions: altitude, humidity, pressure and temperature—this is probably used to correct the volume formulae applied by the device, though we have found very little detail in the technical documentation.

To compare our results to spirograms¹, we performed both the SLP and spirometer measurements while subjects were breathing (see figure 4.1).

The validation of our technique was done by comparing estimations of the lung volume changes from the two different techniques on three male subjects of various anatomies (see table 4.1).

After the system had made a zero flow calibration, the subject was asked to hold the spirometer head in the left hand, left elbow abducted so that the arm and cabling did not obstruct the camera image of the projected grid. He was then asked to start breathing in a relaxed and forced manner through the filter mouthpiece attachment in three different positions: standing,

¹A spirogram is a graph of respiratory movements from spirometry data.

subject	height (cm)	weight (kg)	age	BMI ¹	BSA ² (m^2)
1	175	65	23	21.2	1.79
2	182	79	26	23.8	2
3	180	92	33	28.4	2.12

Table 4.1. Subjects's anatomy data.

sitting and lying; this was done in order to assess the repeatability of the data collected under various conditions.

We deliberately asked the subjects to breathe in a regular tidal breathing fashion to reduce the optimisation time by decreasing the number of parameters to optimise over, while not compromising the validity of comparing the SLP and simulation results for validation purposes. Moreover, only the first 18 seconds (equivalent to 1000 samples as we normalise the data to 56 Hz) of the data were kept to reduce the computation of the cost function during the optimisation process.

4.2. Preparing the data for comparison

The SLP system and pneumotach do not measure the same quantity and therefore direct comparisons are not possible. In order to make a meaningful comparison the SLP data and spirometry data have to be normalised.

SLP collects measurements at a rate of 56 Hz and so this is used as our simulation sample rate; on the other hand, spirometry operates at 100 Hz (see figures 4.2(a) and 4.2(b)). This means that while the curves represent data collected over the same period of time, the spirograms have 100/56 times more samples than the SLP data. Thus, we must re-sample and interpolate the spirometer data such that it is effectively sampled at a rate of 56 Hz. This is done in Matlab using the function `resample` (see figure 4.2(c)).

The simulation gives the volume changes of the thoracic cavity $V_{thoracic\ cavity}(t)$, by subtracting the volume of the abdominal cavity from the total volume. Nevertheless, what the spirometer records is the volume flow of air at the exit of the mouth which is supposedly the volume flow of the lungs $V_{lungs}(t)$. Thus, what we need to compare to spirograms are the volume changes of the lungs from the simulation. As the lungs are contained within the thoracic cavity, their volumes are a ratio of the thoracic cavity (that could possibly vary from one patient to another, this will be discussed in section 4.4.4). To find this ratio, we used the *3D Google Body anatomic model* [38] which is based on the data from Zygote Media Group 3D [39], and measured the different volumes of the big organs within the thoracic cavity (heart, ventricles, aorta, vena

¹Body Mass Index.

²Body Surface Area.

cava, esophagus) and the total volume of the cavity to deduce the ratio of the volume taken up by the lungs in this model. We found a ratio of 25 %. Thus, we multiply the volume of the thoracic cavity given by our simulation by 75 % to obtain the volume of the lungs to be compared to spirograms (see figure 4.2(d)).

Another issue that needs to be addressed is that the spirometry only measures the volume of air that is blown in and out from the mouth, which is in fact the volume flow of the lungs, whereas the simulation provides the variations of the absolute volume of the lungs. The consequence of this is that spirograms at time 0 start with a volume of value 0 and record the variations of air from this point, whereas the simulations at time 0, have a value that corresponds to the volume of the lungs at rest and give the variations of the volume of the lungs from this point. To correct for this, we added the mean of the simulation data to the spirograms (see figure 4.2(e)).

Finally, we must consider the fact that the SLP and spirometry data collection do not begin at precisely the same point in time as each technique is triggered manually and not synchronised at the beginning of the acquisition. To correct for this, we calculate the cross-correlations between the simulation data and the spirometry data over a lag of ± 100 frames. We then find the lag which has the highest correlation, and adjust our data so that the highest correlation is at lag 0 (see figure 4.2(f)).

The different processed curves we obtained for each subject are available in appendix A.

4.3. Optimisation process and data analysis

The optimisation operates over the phases and magnitudes of the activations of the muscles of the rib cage and the abdomen. The breathing frequency f_b , is computed beforehand via a simple analysis of the fitting error over time; saving us one parameter to optimise over. We also assume that the activation functions are sine waves as they have been widely used in previous physically-based modelling of breathing work [4, 3, 12] and have the great advantage of having few parameters to optimise over, which saves us considerable computational time. These assumptions will be questioned later on in this chapter.

4.3.1. Performances of the optimisation

The results of the first step which consists of fitting the skin mesh to the datasets are summarised in table 4.2. What we can infer from this is that the skin fitting process decreases the initial fitting error FE_{ini} , on average by $31 \% \pm 6.5 \%$, leading to an average fitting error of $0.47 \text{ cm} \pm 8.0 \%$ per grid point.

In addition, the optimisation step gives satisfactory results for the average cost function values, $f_{error\ optim}$ of $0.34 \text{ cm} \pm 6.7 \%$ per grid point over the whole sequence. Only (subject 2,

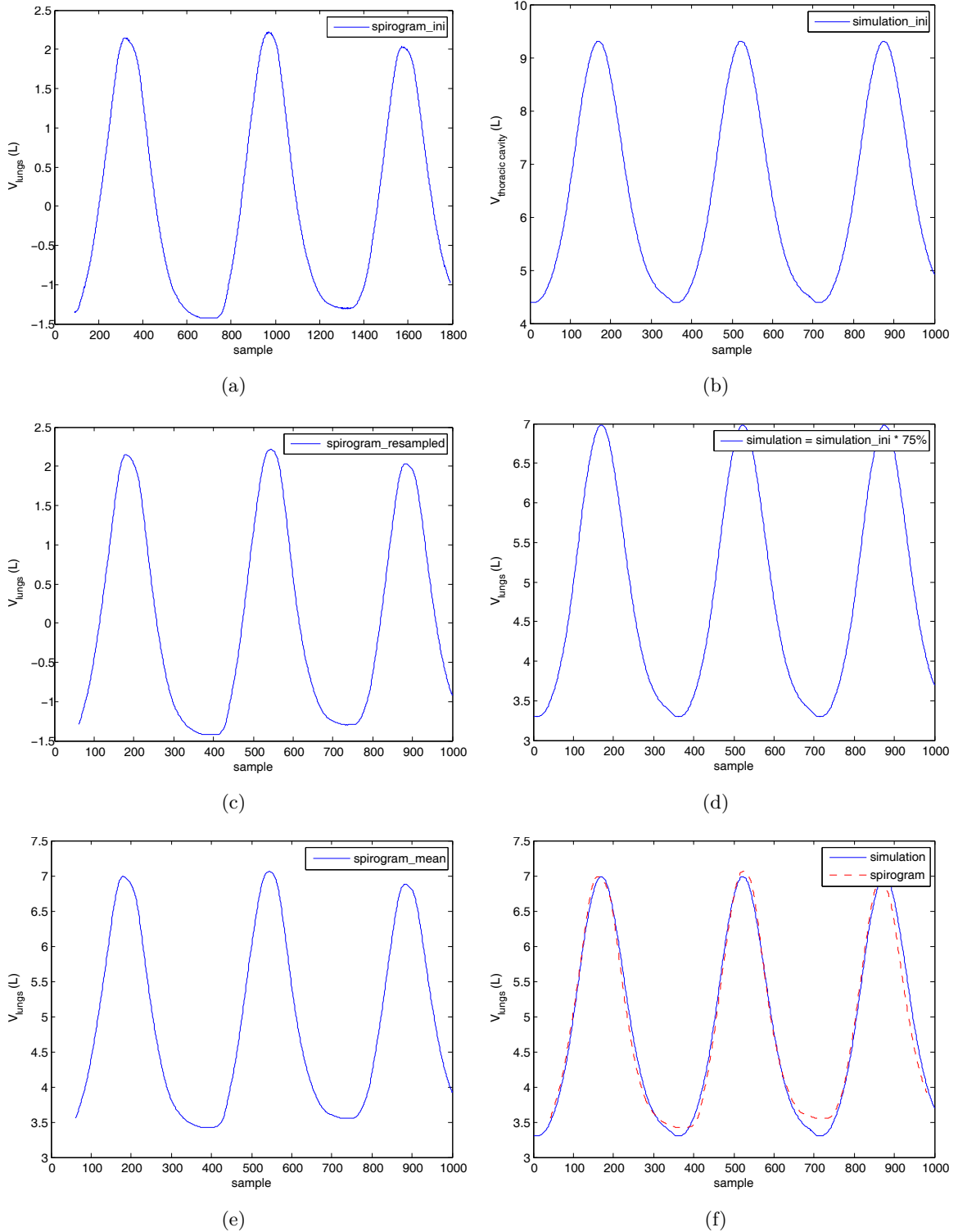


Figure 4.2. Preparation of the simulation and spirometry data before comparison for (subject 1, standing, forced). (a) the raw spirometry and (b) simulation curves have to be processed in order to compare them. Firstly, (c) the spirogram has to be resampled at 56 Hz. Secondly, (d) we take off 25 % of the simulation volume curve to get the lung volume instead of the variations of the thoracic cage volume. Thirdly, (e) we add the mean of the simulation volume curve to the spirogram to get the absolute volume changes of the lungs. Finally, (f) we operate a cross-correlation algorithm to adjust the starting time of the simulation and spirometry curves.

subject	position	breathing style	FE_{init}	FE_{fitted}	$f_{error\ optim}$	iterations
1	standing	quiet	0.6645	0.4230	0.3722	71
		forced	0.7453	0.5286	0.3276	50
	sitting	quiet	0.7402	0.3973	0.2679	63
		forced	0.7947	0.5840	0.3617	56
	lying	quiet	0.6108	0.4509	0.2567	68
		forced	0.8562	0.6083	0.3894	47
2	standing	quiet	0.5463	0.3369	0.2106	54
		forced	0.6145	0.4972	0.4580	72
	sitting	quiet	0.7393	0.4824	0.3505	50
		forced	0.6533	0.4004	0.3725	66
	lying	quiet	0.6207	0.4734	0.3836	68
		forced	0.6612	0.4169	0.3216	61
3	standing	quiet	0.5112	0.3665	0.2899	43
		forced	0.8317	0.5927	0.3729	66
	sitting	quiet	0.6198	0.4531	0.3913	57
		forced	0.6067	0.4159	0.3105	68
	lying	quiet	0.5705	0.4107	0.2427	45
		forced	0.8585	0.5661	0.4427	71

Table 4.2. Improvement provided by the skin fitting process over the skin error among different subjects breathing in different positions. The initial fitting error is given by FE_{init} in cm, after fitting and smoothing the skin mesh as described in chapter 3 we obtain a new fitting error given by FE_{fitted} (cm). $f_{error\ optim}$ (cm) is the cost function value after optimisation, which is mathematically-wise the average of the fitting error when the skin mesh is deforming according to the optimised activations of the muscles over all the frames of the sequence.

standing, forced) and (subject 3, lying, forced) cost function values were above 0.4 cm, which is slightly bigger than the others.

As we might expect, the fitting error is bigger for the forced breathing ($0.51\text{ cm} \pm 8.3\%$) compared to the quiet breathing ($0.42\text{ cm} \pm 4.9\%$), as the movements of both the thoracic and abdominal cavity are supposed to be larger; but interestingly enough, the cost function value for the forced breathing ($0.37\text{ cm} \pm 5.1\%$) and the quiet breathing ($0.31\text{ cm} \pm 6.8\%$) are both low and similar. This means, that the optimisation process does not do significantly worse when it comes to fitting larger breathing movements compared to calmer ones.

4.3.2. Analysis of the optimisation outputs

Table 4.3 shows the exploitable outputs of the optimiser: the activation phases of the rib cage and abdomen (ϕ_{rc} and ϕ_{abd}) and the activation ratios for the ribs and diaphragm, which are the

subject	position	breathing style	$\Delta_\phi = \phi_{abd} - \phi_{rc}$	A_{ribs} (%)	$A_{diaphragm}$ (%)
1	standing	quiet	0.21	23	26
		forced	-0.051	37	41
	sitting	quiet	0.011	23	25
		forced	-0.0031	38	42
	lying	quiet	-0.39	8	48
		forced	-0.2	35	51
2	standing	quiet	0.012	15	21
		forced	3.9	35	31
	sitting	quiet	0.16	12	20
		forced	-1.4	28	23
	lying	quiet	0.013	3	12
		forced	-0.053	23	25
3	standing	quiet	0.50	15	13
		forced	-0.44	26	51
	sitting	quiet	0.071	25	31
		forced	1.6	31	49
	lying	quiet	-0.051	2	8
		forced	-0.32	12	32

Table 4.3. Optimal parameters found for the different datasets. ϕ_{rc} and ϕ_{abd} are the activation phases of the rib cage and abdomen respectively. A_{ribs} and $A_{diaphragm}$ correspond to the activation ratio of the maximum reachable magnitude of the rib muscles and the diaphragm respectively.

ratios of the observed activations and the maximum reachable magnitudes of the rib muscles and diaphragm: A_{ribs} and $A_{diaphragm}$ respectively.

Phase shift between the abdominal and rib cage cavities

The absolute value of the phase shift $|\Delta_\phi| = |\phi_{abd} - \phi_{rc}|$ indicates how much the abdominal cavity and the rib cage movements are out of phase; its sign $sign(\Delta_\phi)$, indicates which muscle group is fired first: if it is positive, the diaphragm is fired before the inspiratory muscles of the rib cage, otherwise it is the contrary.

We can make some observations on the results:

1. During quiet breathing in 7/9 of the cases, $\Delta_\phi > 0$: the diaphragm is fired first.
2. During forced breathing in 7/9 of the cases, $\Delta_\phi < 0$: the rib cage is fired first.
3. The value of the phase shift is bigger during quiet breathing than during forced breathing in 6/9 cases.

4. The (subject 2, standing, forced) phase shift is nearly π which tells that the diaphragm and the inspiratory muscles are nearly completely out of phase resulting in asynchronous breathing² leading to poorer ventilatory mechanics which can cause serious respiratory illnesses.

Points 1, 2 and 3 are *en accord* with the study carried out by Sharp et al. [40] on the relative contributions of rib cage and abdomen to breathing in normal subjects. According to [40], the rib cage is capable of more rapid contractions than the abdomen. As a consequence, for rapid manoeuvres such as forced breathing, intercostals and scalene muscles are called into action before the diaphragm; whereas during slow breathing, the diaphragm is nearly always fired before the rib cage muscles which is a trend we can observe in the results obtain.

Point 4 brings up an intriguing result as (subject 2, standing, forced) is not consistent with the other measurements taken from subject 2. If subject 2 had asynchronous breathing it would have affected all the measurements taken and subject 2 would not be in a healthy condition, as he indeed was. Looking more closely at the SLP data, we can definitely see an asynchronous breathing style in this specific position. The grid points of the SLP grid in the central part of the abdominal area are clearly out of phase compared to the grid points in the rib cage area. There were no obvious reasons for this abnormal breathing style except that subject 2 can willingly favour either his rib cage or abdomen to breathe and that while actively thinking about breathing normally in front of the SLP device, he might have produced an unnatural rather than an ordinary breathing style. More measurements on subject 2 were taken to test the reproducibility of the phenomenon, but we found no evidence of asynchronous breathing.

Relative contributions from the abdominal and rib cage cavities

A_{ribs} and $A_{diaphragm}$ are the activation ratios of the observed activations to the maximum reachable magnitudes of the rib muscles and the diaphragm respectively found by the optimiser to fit the SLP data. They are an indication of the strength of the forces exerted by the muscles of the different cavities but cannot be compared to each other in terms of movement induced by the cavities on the external part of the body: having an A_{ribs} of 40 % and an $A_{diaphragm}$ of 60 % does not necessarily mean that the motion of the abdominal area will be significantly bigger than the rib cage. In 15/18 of the cases in table 4.3, $A_{diaphragm}$ was bigger than A_{ribs} which probably indicates one of two scenarios. The first is that all three subjects use the muscles of the diaphragm more than those of the rib cage. The second, and more likely, is that the result is simulation-dependent; the simulated diaphragm possibly needs a greater input to produce movement than the rib cage (which is linked to either the number of muscles used, the parameters of the different muscles, or the maximum value for the activation of the different muscles).

²Asynchronous breathing, also known as inverse breathing or paradoxical breathing, consists of expanding the abdomen while breathing out, and then compressing it while inhaling—the opposite of what an abdomen would do during natural breathing.

From the study detailed in [40], points of particular interest are:

1. There are no major differences between men and women or between the young and the elderly during any respiratory acts.
2. During quiet breathing most normal subjects are abdominal breathers when supine and thoracic breathers when upright (standing and sitting).
3. Rapid manoeuvres are accomplished with a bigger contribution from the rib cage than from the abdomen.
4. During forced breathing it appears that abdominal and rib cage muscles act to optimise the mechanical advantage of the diaphragm.

Considering the precautions we have to take concerning any comparison between A_{ribs} and $A_{diaphragm}$ explained previously, we can however note that during quiet breathing in supine A_{ribs} and $\frac{A_{ribs}}{A_{diaphragm}}$ have their lowest values than in any other position. This suggests first, that there is a smaller contribution from the rib cage while supine during quiet breathing than in any other position, secondly that the abdomen contributes significantly more than the rib cage in this configuration which is in accordance with point 2.

Concerning point 3, we can also see that the ratio $\frac{A_{ribs}}{A_{diaphragm}}$ during quiet breathing over all positions is on average $0.64 \pm 34\%$ and $0.81 \pm 28\%$ during forced breathing. What can be deduced from this is that the contribution of the rib cage compared to the abdomen during forced breathing is in proportion higher than during quiet breathing; which is precisely what point 3 highlights.

4.4. Comparing simulation and spirometry data

Commonly, methods to assess agreements between two techniques of pulmonary function testing have relied on tools such as correlation coefficients, tests based upon pairing one's data and calculating the mean of the differences between the two methods, and the use of Bland-Altman plots to set a 'limit of agreement' based on one's data. This section will detail the results obtained with correlation coefficients and what can be inferred from them. Then, it will highlight the different specificities of Bland-Altman plots which are commonly used in medical statistics and the results obtained with this method. Finally, it will describe a frequentist and a Bayesian test on the null hypothesis that the two methods are equivalent for calculating tidal volumes, operating over both the raw time series data and the extracted parameters: the cosinor model and the BARS (Bayesian Adaptive Regression Splines) method.

4.4.1. Correlation coefficient

The most intuitive way to test whether or not two methods yield the same result is to compute the correlation between the results attained by the two techniques. The correlation coefficient r is a statistic that measures the strength and the direction of a linear relationship between two variables.

Table 4.4 presents the correlation coefficients $r(sim, spir)$ between the simulation and spirometry data for each subject. Note that data for (subject 3, lying, quiet) is omitted; we see in figure A.3 that the spirogram for this patient is abnormal (probably coming from bad handling of subject 3 during the measurement), as a consequence this dataset is not exploitable for comparison purposes and we did not compute the correlation coefficient, it will be omitted in what follows. The average correlation coefficient between the datasets—(subject 3, lying, quiet) omitted—is $0.88 \pm 5.8\%$ which corresponds to a *strong* correlation between the simulation and spirometry data.

Nonetheless, we have to bear in mind that the correlation coefficient has several flaws. First, it does not depend on the scale on which the data were collected and cannot be used in determining agreement between measurements when scale is of importance, as it is in our case (our main goal being finding the changes of the absolute volume of the lungs). Second, as explained by Bland and Altman [41], correlations depend solely on the variance between the true values and the variances of the methods, with low correlations potentially being obtained simply due to large amounts of noise within one's data. They also assert that correlation merely measures a relationship between the data and not an agreement.

The correlation coefficient method determines at a basic level that two methods are related. As a result, what we can reasonably infer from the high correlation coefficient values obtained, is that simulation and spirometry methods are related and give similar data. However, more refined methods have to be sought in order to validate our model.

4.4.2. The Bland-Altman plot

The Bland-Altman plot is an analytical tool proposed by Bland and Altman [41, 42] to serve as a basic visual indicator of agreement between two methods. In fact, it is a plot of the difference between measurements using the two methods versus the average of the two measurements using both methods. Thus, a Bland-Altman plot provides a visual way to spot systematic errors. A dashed-dotted line for zero mean difference along with two dashed lines at $Mean_{diff} \pm 1.96 \times SD_{diff}$ are included in the plot. $Mean_{diff}$ is the mean of the difference between the two measurements, ± 1.96 corresponds to the points in between which a $\mathcal{N}(0, 1)$ distribution integrates to 0.95 defining the ‘limit of agreement’ and SD_{diff} is the standard deviation of the difference between the two measurements. Bland and Altman’s assertion is that if the methods agree, then 95 % of the points on said plot will fall within those confidence

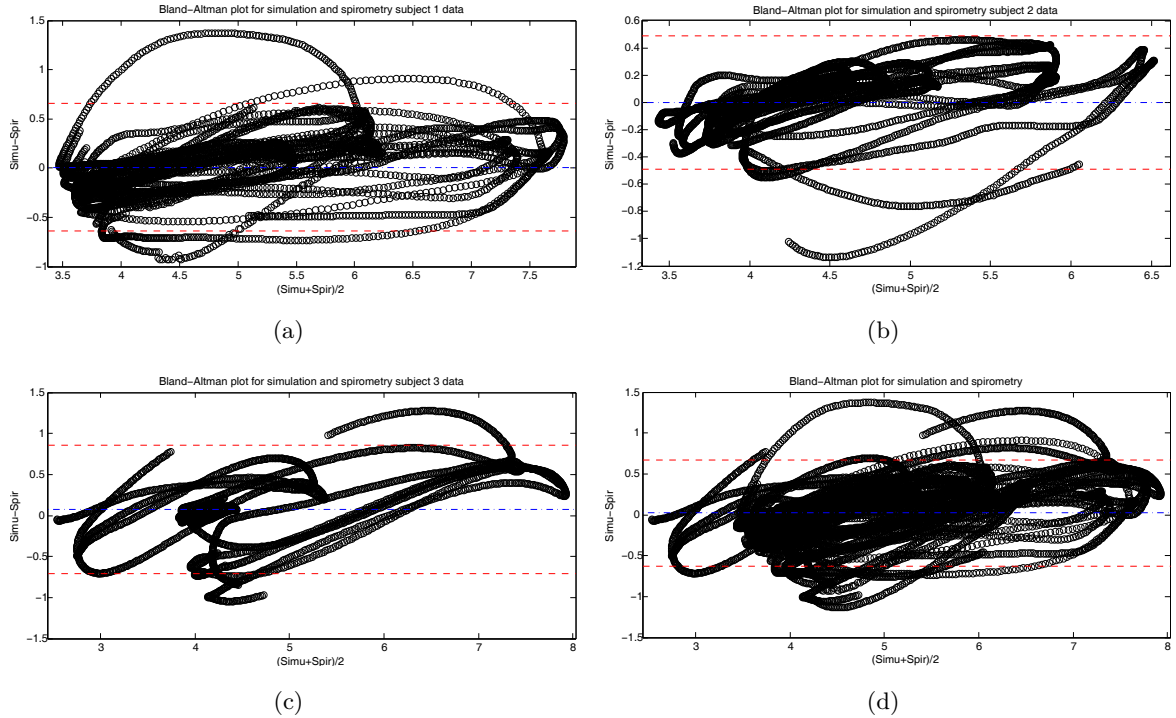


Figure 4.3. Bland-Altman plots for spirometry and simulation data. The blue dashed-dotted line corresponds to the zero mean difference and the red dashed lines to $\pm 1.96 \times SD_{diff}$ from the mean in either direction defining the limits of agreement. (a), (b) and (c) are the Bland-Altman plots for all measurements for subjects 1, 2 and 3 respectively. (d) is the Bland-Altman plot for the all data from all subjects.

bounds.

The different Bland-Altman plots we obtained for each experiment are available in appendix B. Figures 4.3(a), (b) and (c) present the Bland-Altman plots of all measurements for a single subject and figure 4.3(d) for the whole dataset. The Bland-Altman plots obtained present systematics due to the fact that the points in our data are causally correlated.

One can see that the Bland-Altman plots from our data give very good results with few points outside the Bland-Altman ‘limits of agreement’, which is in keeping with the null hypothesis that the simulation and spirometry methods are the ‘same’. Thus, we can say that not only simulation and spirometry give similar results (as the correlation coefficient study showed in the previous section) but also that these two methods are measuring the ‘same’ data (volume changes of the lungs). The question then arises as to whether the simulation and spirometry methods are **equal** and whether the Bland-Altman plots can provide an answer to this. According to Fogarty [43], the Bland-Altman plot is a useful reference for assessing equality between two methods, however it should only be considered as a visual aid or starting point in assessing strict equality between two methods. Moreover, Bland-Altman plots suffer from several flaws. For instance, the upper limits of the Bland-Altman plot will increase in range proportional to the magnitude of the variance. Thus, methods that vary from one another

quite drastically but have an average difference of around 0 will seem perfectly acceptable based on the ‘limits of agreement’. To cope with the inherent flaws of Bland-Altman plots in assessing the **equality** between two methods, [43] derived testing techniques dealing with the underlying nature of the raw data from spirometry and SLP using the cosinor and BARS methods. These methods exploit the fact that rather than merely having one data point per subject, each collection of data results in a set of two time series, each containing hundreds of data points.

4.4.3. The cosinor model

The cosinor model presented by Nelson et al. [44] is a way of utilising the known sinusoidal nature of a dataset and, given a set of known periodicities, fitting a series of cosine curves to the data using least squares regression. In fact, it fits the model according to the following relationship given in [45]:

$$f(t) = M + \sum_{i=1}^C A_i \cos(\omega_i t + \varphi_i) + \epsilon(t) \quad (4.1)$$

where M is an intercept coefficient, A_i and φ_i are coefficients to be estimated, ω_i are known frequencies obtained beforehand using a method such as Fast Fourier Transform, $\epsilon(t)$ is noise assumed to be IID $\mathcal{N}(0, \sigma^2)$ and C is a user defined number of cosine curves to fit. For our purposes, we found that $C = 4$ provided our fits with sufficiently accurate features while still maintaining parsimony.

For each cosine curve, we have two unknown parameters A_i and φ_i which must be calculated based upon the optimal fit to our data. We thus have a vector of parameters $\Theta = [M \ \beta_1 \ \gamma_1 \ \dots \ \beta_C \ \gamma_C]$, where $\beta_i = A_i \cos(\varphi_i)$ and $\gamma_i = -A_i \sin(\varphi_i)$, to estimate. For both the simulation and spirometry data, the vector of parameters Θ_{simu} and Θ_{spir} are estimated using a Multivariate Least Squares Regression.

Figure 4.4 shows a curve produced by the cosinor model to fit one of our simulation volume curves.

The idea behind the cosinor model derived in [43] is to compare the parameter vectors to test the equality of the two methods assessed. [43] extends the cosinor model’s derivation to a test of equality between two time series and adapts the said test to spirometry and SLP data. Table 4.4 reports the p -values associated with these tests for each of our datasets. The p -value serves as an indicator of evidence against our null hypothesis. [43] uses the standard threshold of $\alpha = 0.05$ for determining if we can reject the null hypothesis that the coefficient vectors are the same. Furthermore, it has to be said that rather than finding out how likely it is that our null hypothesis is true, the frequentist hypothesis testing, which is at the heart of the cosinor method, calculates how unlikely a certain result is, given that our null hypothesis is true. For

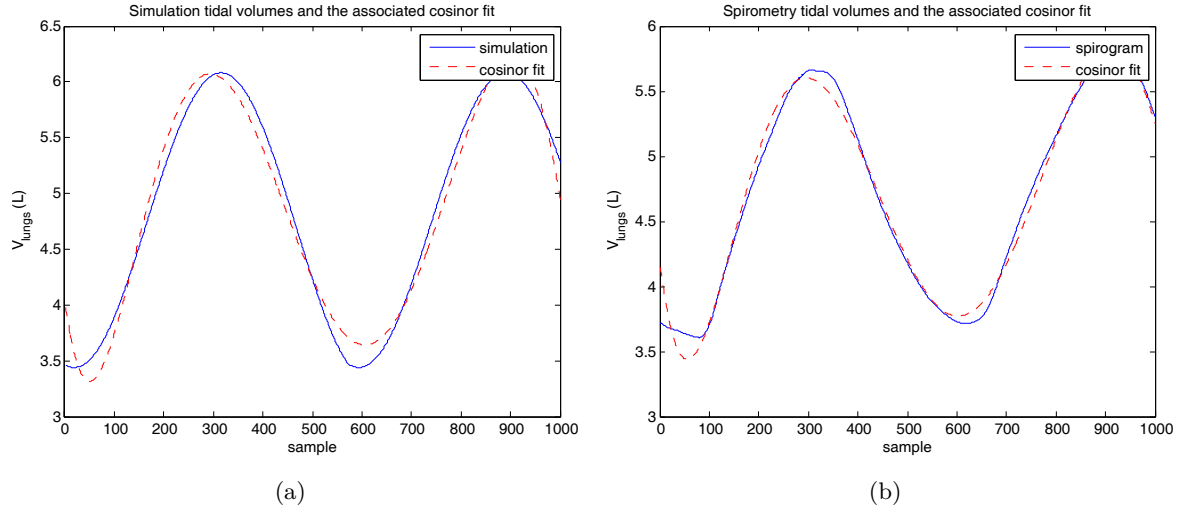


Figure 4.4. Volume-time curves for (a) our simulation and (b) spirometry data (blue lines) and the corresponding cosinor fits (red dashed lines).

an in depth description of assumptions and mathematics behind this technique, please consult the Master's thesis of Colin Fogarty [43].

For our data collection, we find that of the 17 comparisons—(subject 3, lying, quiet) being omitted as justified in 4.4.1—, four of them ((subject 1 & 3, standing, quiet), (subject 1, sitting, quiet) and (subject 3, lying, forced)) provide a p -value low enough to reject the null hypothesis. We will now investigate why these comparisons rejected the null hypothesis:

1. Looking at the simulation and spirometry curves for (subject 1, standing, quiet) in appendix A.1, we see that the spirogram at time [150, 200] suffers from a variation that does not seem to be realistic and that could have appeared for many diverse reasons and also that there is a scale discrepancy. These facts led to a poor cosinor fit for the spirogram and thus would explain why the low p -value was obtained.
2. (Subject 1, sitting, quiet) does not appear to suffer from a poor cosinor fit. Comparing the curves more closely however, one can see that the spirogram and the simulation are slightly out of phase. This is due to the periodic nature of the activation inputs of the muscles. As explained in section 4.3, we optimised over sine function parameters as inputs to the respiratory muscles of the model to fit the SLP data, and worked on the assumption that the breathing style of each measurement was steady. As a consequence, the simulation data are periodic curves optimised to the SLP data. Although this is unlikely to be perfectly true all of the time, it is interesting to note that all other data is regular and periodic. As a consequence, we believe that the phase shift between the spirogram and the simulation curve was the main reason for the rejection of the null hypothesis in this case.
3. (Subject 3, standing, quiet) and (subject 3, lying, forced) show less conventional types

of breathing. The shape of the spirograms can clearly be better described as a sawtooth shape rather than a sine wave shape (see A.3). Even though there are no obvious direct reasons that might explain this particular type of breathing, subject 3's general practitioner advanced the possibility that the *polycystic kidney disease* that subject 3 has been suffering from, might explain this. A polycystic kidney disease is a cystic genetic disorder of the kidneys characterised by the presence of multiple cysts. The cysts are numerous and are fluid-filled, resulting in massive enlargement of the kidneys [46]. This enlargement could possibly exert an extra pressure on the diaphragm and thus alter the breathing style. This breathing pattern has previously been seen in a number of people, who were not obviously suffering from any kidney disease. Nevertheless, this non-standard type of breathing is not perfectly reproduced by the simulation and this is clearly the reason why the null hypothesis was rejected for these datasets. It is important to note that the cosinor fitting to the spirograms was better in these cases than the others taken from subject 3 that have a 'sawtooth'-like shape but which were not rejected. Looking at the spirogram more closely, the coefficient vector from the cosinor fit of the spirogram Θ_{spir} had more variable sine parameters which were not present in the coefficient vector of the cosinor fit of the simulation Θ_{simu} . This could explain why the other curves did not fail to reject the null hypothesis (the coefficient vectors only having the core low variation sine parameters) and why these two rejected the null hypothesis.

Thus, the reasons why these four datasets rejected the null hypothesis rely on either artefacts in data, non-periodic signals or non-conventional types of breathing, therefore pointing out limitations of the simulation technique. The factors that cause pairs to reject the null hypothesis according to the correlation and/or Bland-Altman studies are not obvious, but the cosinor model brings a better and more accurate understanding of the degree of similarity between data. From our data, we can see that the majority of our tidal volume curves fail to reject the null hypothesis that the two curves are the same. As a result, what we can say from the cosinor study is that the extracted cosine parameters from the simulation and the spirometry data are most of the time unlikely to be different. In other words, simulation and spirometry data coincide in their sinusoidal features.

However, as said previously, the frequentist approach provides no means of computing a concrete probability that one's null hypothesis actually is true, which is ultimately what a comparison study would like to show, but it is rather set up as a proof by contradiction.

4.4.4. BARS: Bayesian Adaptive Regression Splines

Unlike the frequentist approach, the Bayesian paradigm attempts to calculate how likely the null hypothesis is. In our quest to test our null hypothesis that tidal volume curves produced by simulation and spirometry are the same, we now present an extension of a recently introduced method of curve fitting called Bayesian Adaptive Regression Splines (herein abbreviated as BARS) to give a test for equality of our two functions.

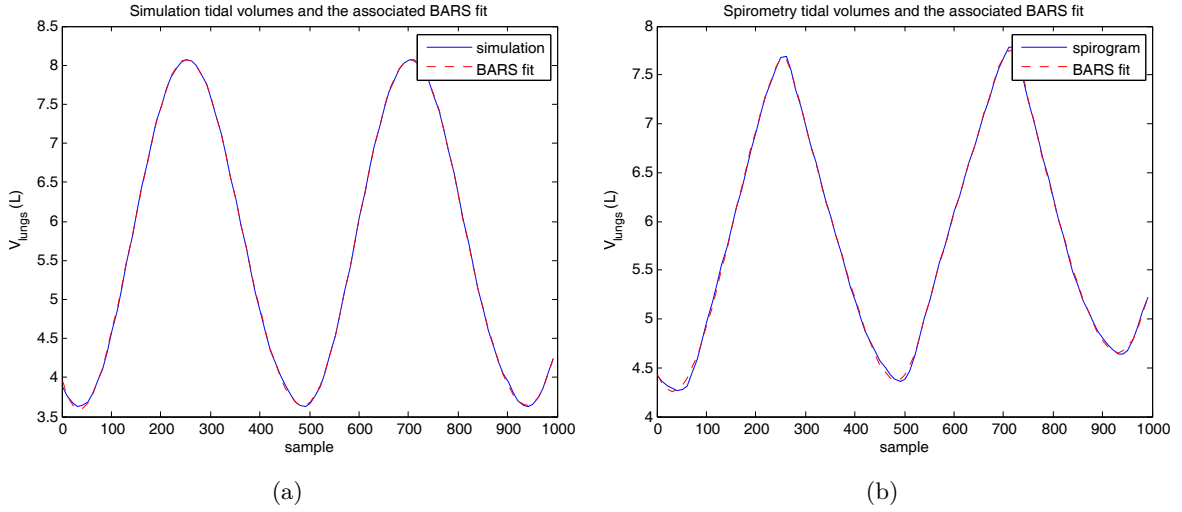


Figure 4.5. Volume-time curves for (a) our simulation and (b) spirometry data (blue lines) and the corresponding BARS fits (red dashed lines).

BARS is a Bayesian method for fitting curves to data based on a ‘signal plus noise’ model developed by DiMatteo et al. [47], of the form:

$$y_j = f(x_j) + \epsilon_j \quad (4.2)$$

This method uses B(asis)-Spline design matrices to fit splines of the third degree to data, and uses a reversible jump Metropolis-Hastings Markov Chain Monte Carlo simulation to select the location of the knots. The algorithm works by starting with an initial knot set specified by an uniform distribution on the location of these knots to be denoted as $\xi_{current}$, an initial number of knots $k_{current}$, and the resulting coefficient vector based on this knot set $\beta_{current}$, as well as a maximum number of knots that can be used in fitting the data. Then, with equal probability the algorithm decides to either generate a new knot, delete an existing knot or relocate a knot to a new position and thus creates a new knot set, number of knots and coefficient vector $\xi_{candidate}$, $k_{candidate}$ and $\beta_{candidate}$ respectively. Next the acceptance probability for the candidate knot set is calculated. If the acceptance probability $P(accept)$ is 1, then the new knot set is accepted making it the incumbent in subsequent runs of the MCMC. If it is < 1 , then it accepts the new knot set with probability $P(accept)$. After running the simulation numerous times (for our data we do this 2000 times after an initial ‘burn-in’ period of 200), we arrive at a B-spline design matrix that fits the data extremely well. Figure 4.5 shows one of our tidal breathing sets with the corresponding fit produced by BARS using 10 knots overlaid.

Forgarty [43] then uses the method outlined by Behseta and Kass [48], which gives a means by which BARS can be modified such that it can be used to test equality of two curves in a Bayesian framework. Then he exploits the fact that BARS can simultaneously fit two curves and then compute the coefficient vector for fits of each dataset individually and for a fit of the two datasets simultaneously by restricting the curves to having the same knot set ξ . Based on

this, he conducts a hypothesis test adapted to spirometry and SLP comparisons. The method tests whether the function that BARS fits to the first curve (simulation data) is the same as that fit to the second curve (spirometry data), by comparing how likely the joint fit of the two datasets is, relative to the likelihood of the fits of the two curves individually, with the constraint that the fits have used the same knot set. The null and alternative hypotheses being:

$$\begin{aligned}\mathbf{H}_0 : f_{spir}(t) &= f_{simu}(t) \\ \mathbf{H}_a : f_{spir}(t) &\neq f_{simu}(t)\end{aligned}\tag{4.3}$$

The posterior probability $P(\mathbf{H}_0 | simu, spir)$ of \mathbf{H}_0 is then computed based on the following:

$$P(\mathbf{H}_0 | simu, spir) = \mathbb{E}[P(\beta_{simu} = \beta_{spir} | \xi, simu, spir)]\tag{4.4}$$

For the full details of the calculation and methodology, please refer to [43].

Table 4.4 shows our calculations of $P(\mathbf{H}_0 | simu, spir)$ for our data. Looking at these values, we see that of the 17 pairs tested, two produced a strong probability (of 1 and 0.86) that the null hypothesis is true, 14 produced extremely low probabilities and the remaining one is in the middle giving a 0.18 probability. Comparing these probabilities to the cosinor p -values also displayed in 4.4, we see that the datasets which reject the null hypothesis for the cosinor model do not necessarily have low values of $P(\mathbf{H}_0 | simu, spir)$ for our BARS comparison and vice-versa. For instance, (subject 2, standing, quiet) has a p -value of 0.95 which is the highest achieved in our dataset and an infinitesimal $P(\mathbf{H}_0 | simu, spir)$ equal to 10^{-90} . Conversely, (subject 1, standing, forced) gave a $P(\mathbf{H}_0 | simu, spir)$ of 1 and a p -value of 0.57. This exemplifies the fact that the cosinor and the BARS methods do not assess the same features in comparing two datasets.

Our results tend to provide substantial evidence against our null hypothesis as very few comparison results were positive. From the BARS study we can deduce that the simulation and the spirometry do not provide the same data at a precise level. Several reasons could be explored to explain this conclusion:

1. The BARS method tests the likelihood that two data are precisely the same and as such is very discriminative, whereas the cosinor tests the similarity of the data based on their frequency features—and we have seen that the simulation and the spirometry are very similar via the frequentist approach.
2. We made several assumptions for the optimisation process that can now be discussed. First, we used sine functions as inputs to the muscle activations, which is what has commonly been done in previous work on physically-based modelling [4, 3, 12]. Even though the data obtained are very **similar** to spirometry as the correlation, Bland-Altman and

cosinor studies showed, the results obtained with the BARS technique exposed that they are **not exactly the same** (the comparisons which rejected the cosinor tests were already indicating this fact). We believe that this is due to the true nature of the inputs. For instance, we tried to reproduce the sawtooth shape breathing of subject 3 by choosing different type of inputs and it seemed that deformed sine functions with a steeper slope in its ascending and descending part resulted in a simulated lung volume with a more ‘triangular’ shape. One solution would be to optimise over a basis of functions as done in [27], but this is not currently feasible as it would require a huge increase in computational power. A less costly method worth investigation would be to optimise over periodic function parameters similar to sine; it would however inevitably introduce new parameters and significantly increase the optimisation time.

3. Recall that one step in preparing the data for comparison is to take off 25 % of the simulation curve to get the lung volume instead of the thoracic cage volume flow. This figure can possibly vary from one subject to another and affects the amplitude of the simulation data, which could result in poor agreement between the data and which would particularly affect the BARS method. To the best of our knowledge there are no non-invasive methods to accurately measure this figure.

subject	position	breathing style	$BARS(simu, spir)$	$COS(simu, spir)$	$r(simu, spir)$
1	standing	quiet	0.18	0.035	0.78
		forced	1	0.55	0.97
	sitting	quiet	10^{-11}	0.0068	0.89
		forced	0.86	0.57	0.91
	lying	quiet	10^{-107}	0.71	0.94
		forced	10^{-100}	0.11	0.97
2	standing	quiet	10^{-90}	0.95	0.91
		forced	10^{-150}	0.81	0.82
	sitting	quiet	10^{-116}	0.91	0.91
		forced	10^{-42}	0.62	0.95
	lying	quiet	10^{-108}	0.060	0.87
		forced	10^{-146}	0.23	0.91
3	standing	quiet	10^{-27}	0	0.82
		forced	10^{-42}	0.53	0.88
	sitting	quiet	10^{-75}	0.44	0.81
		forced	10^{-89}	0.088	0.82
	lying	quiet	err	err	err
		forced	10^{-66}	0.021	0.86

Table 4.4. The $BARS(simu, spir)$ column corresponds to $P(\mathbf{H}_0 \mid simu, spir)$ which is the result of the BARS hypothesis test on the simulation and spirometry tidal volumes. The $COS(simu, spir)$ column corresponds to the p -value of the cosinor method equality test between the simulation and spirometry data. The $r(simu, spir)$ column corresponds to the correlation coefficient between the simulation and spirometry data.

5

Implementation Issues

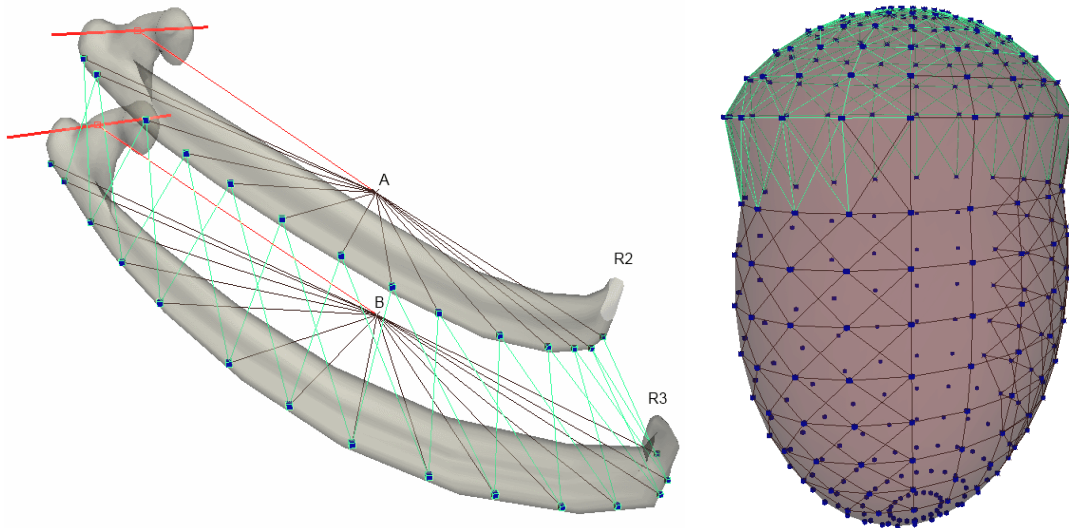
This chapter explains how we implemented our method and the different software and file types used.

5.1. Joints and muscles

To construct our model, we used the 3D animation software Autodesk Maya and MEL (Maya Embedded Language) scripting. As an initial basis, we used the polygonal skeleton model described in chapter 1; we then divided it into its constituent parts: ribs, sternum, vertebrae and intervertebral discs. These different parts were made rigid so that constraints can be applied to them; we have also assigned physiology-based masses using data given by [11] (see table 1.1). In addition, we modelled the joints linking the different rigid parts as already detailed in chapter 1:

vertebrae (C1–C7, T1–T12, L1–L5): ball joints whose centres are located at the middle of the segment defined by the centres of mass of adjacent vertebrae; simulating the intervertebral discs joint function.

vertebrae (T1–T12) – ribs (R1–R12): hinge joints crossing the *articular facets for the trans-*



(a) Muscle and joint structures between rib 2 and rib 3. (b) Muscle structure in the abdominal cavity.

Figure 5.1. (a) muscle and joint structures between rib 2 and rib 3. Hinge joints (red) connect each rib and their associated vertebrae. The intercostal muscles are modelled as springs (green) and each muscle connects one node (blue box) to another. Each node is attached to a rib with a pin constraint (brown) at the center of mass of the ribs (points A and B). (b) the abdominal cavity is modelled as a polygonal sphere (brown) where nodes (blue) are attached to vertices. The abdominal muscles connect the different nodes (e.g. the diaphragm, in green, at the top of the cavity).

verse processes of vertebrae and the middle of the *superior articular facet for the vertebral body* and the *inferior articular facet for the vertebral body*.

ribs (R1–R9) – sternum: spring joint simulating the cartilage.

Since the muscle model we used can only connect to the centre of a rigid object, boxes are attached to polygon vertices with a pin constraint (see figure 5.1(a)). To form the different muscles (rib cage and abdominal muscles) we adopted a procedural approach using MEL scripting:

1. Boxes serving as nodes connecting one extremity of a muscle to the other are placed on the different rigid parts of the skeleton.
2. Each box is linked to a rigid part through a pin constraint.
3. The different muscles are added between the nodes.
4. The parameters of the muscles are tuned.

For the abdominal cavity, we used a polygonal sphere whose centre is fixed in space but whose shape deforms due to the displacement of its vertices.

5.2. Abdominal movement

From a modelling perspective, the vertices of the polygonal sphere used to simulate the abdominal cavity are passive at the bottom and the back side, while those on the diaphragm, the lateral and front parts, are active. At each frame, we compute the pressure force (see equation 2.6) for each active vertex with MEL scripting and send the resulting impulse force as an input to the Runge Kutta Adaptive rigid solver. The solver displaces the vertices according to the given impulse and the muscle activations at the next frame.

5.3. Optimisation

The optimisation process requires communication between different programmes. The optimiser is coded in Matlab and acts as the central programme. The SLP data is first converted into ASCII files `slp_markers_#` : for each frame we have a matrix of the different positions of the grid points. Then the following sequence is repeated until we reach a sufficiently low optimisation error:

1. The optimiser (Matlab) computes the set of parameters to test and saves them into a `parameters` file (ASCII).
2. In order to evaluate the cost function, the optimiser sends a request to Maya to launch the animation through a DOS command.
3. Before the animation starts, an MEL scripting programme modifies the different parameters of the simulation according to the `parameters` file.
4. Two other MEL scripting programmes (`rib_cage` and `abdomen`) activate the rib cage and abdominal muscles at each frame and save the coordinates of the vertices associated with the SLP markers in ASCII files (`model_markers_#`).
5. Once the animation is finished, the optimiser computes the cost function by operating over the `model_markers_#` and the `slp_markers_#` files and derives the new set of optimal parameters.

Figure 5.2 summarises the structure of the implementation.

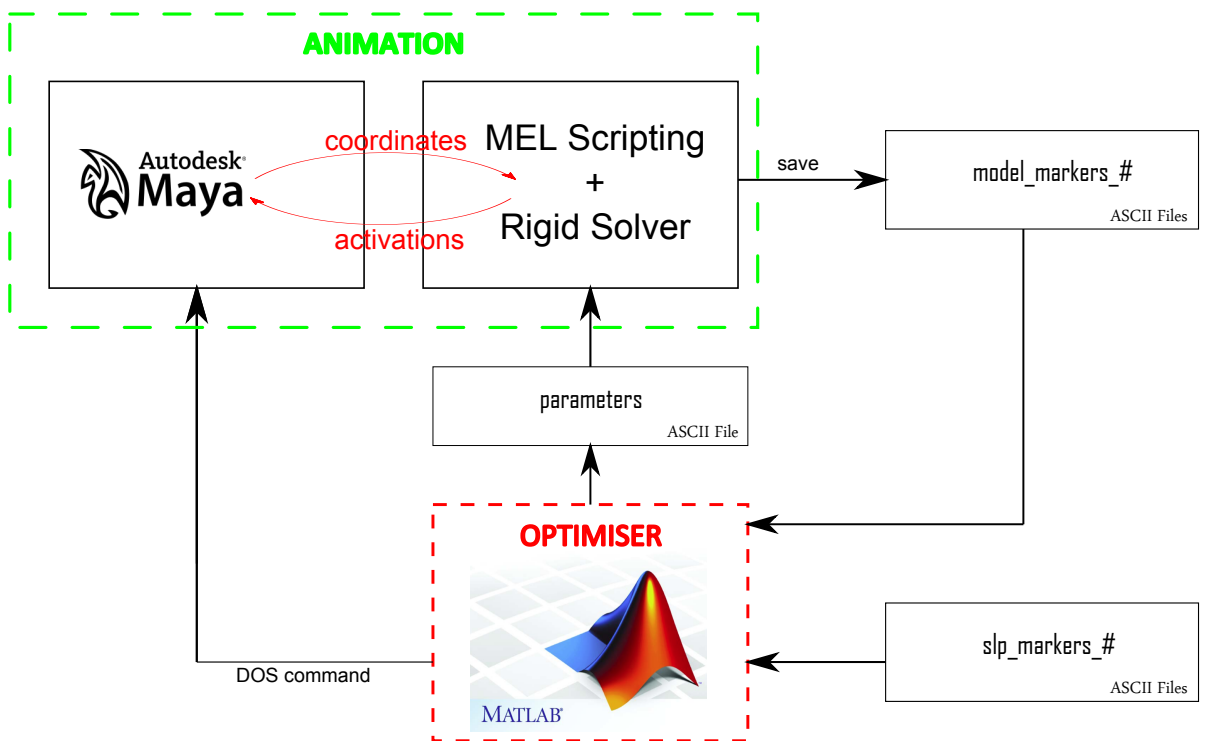


Figure 5.2. Implementation structure of the optimisation process.

Conclusion

Modelling is a field of soaring interest at the interface between engineering and medicine. Accurate modelling has the potential to enhance diagnostic accuracy and efficiency, to provide a better understanding of physiological behaviours in the body with reduced costs and to avoid traditional invasive methods. In breathing, there is a crucial need for a non-invasive means to assess pulmonary function among infants, the elderly, or patients for which conventional procedures would impose a compromise in health; for example, patients in intensive care units.

In this thesis, we presented a novel non-invasive method for performing pulmonary function testing using structured light (SLP), 3D modelling and optimisation algorithms. In contrast to related breathing simulation models, our simulation is geared towards medical applications. As a consequence, our model offers significant improvements and a higher level of sophistication compared to others in the published literature: it has high anatomical accuracy, is fully tunable and can fit different patient anatomies according to various given characteristics. In addition, the optimisation process used to provide data-driven simulations has not previously been well explored. Only DiLorenzo [11] proposed a sketch of a data-driven approach in his *Breathe Easy* model. In addition, we believe it to be very important that our method be rigorously tested for equivalence to another well-acknowledged lung volume measuring technique: spirometry. Thus, we did not only perform the validation exercise using the tools common in most medical comparisons studies, we also utilised state-of-the-art frequentist and Bayesian tests that use the underlying nature and characteristics of our data, providing testing techniques that are much more appropriate. The results themselves provide strong evidence that the simulation and spirometry data are very similar but also point out that they are not exactly the same. Some proposals for future extensions to the work presented are explored below.

Even though the assumptions made about the nature of the activation inputs (sine waves) of the respiratory muscles provide good results for the simulated changes of lung volume, we believe that they are simplifications of the true nature of the respiratory muscle activations. Ideally, we would operate the optimisation over a basis of functions—which could be easily implemented in our code—but the computational power that would be required is for the

Conclusion

moment not available to us.

One advantage of our method is that it offers the possibility to spatially assess breathing patterns. We have already exploited this feature through the natural segmentation of our model: the rib cage and abdomen. This enabled us to analyse the contributions of the different activation magnitudes and phase shifts that operate in SLP datasets. However, we could improve the compartmental analysis further by splitting up the chest wall in many other ways. For example, splitting the chest wall into left-hand and right-hand sides could prove interesting for patients who have suffered from a collapsed lung; or we could isolate specific rib regions to reproduce the breathing style of a patient who had a tumour resection in his chest wall or even a rib replacement. This could be done by selecting the different muscles involved and modifying their different intrinsic parameters and activation inputs.

Additional validation tests need to be performed. In particular, it is desirable that we perform a proper analysis of our method on different ranges of the population: the young, the elderly, women etc. For the moment, we have performed our validation on mostly healthy male subjects but we have all the technical tools in hand to extend our database.

One of the major advantages that the SLP technique brings is that it does not require physical contact with a patient. As such, the system could be used to monitor premature babies inside incubators or animals. To do so, we would need to adapt the rigid skeleton and several muscle layers to fit baby and animal anatomies in order to apply our technique; but the general principle and main steps would be exactly the same.

Another area of future work lies at the implementation of the technique itself. Currently, the optimisation process takes around 10 hours to have a data-driven simulation of 20 seconds. A port of the current Matlab and MEL implementation to compiled C/C++ code and above all, a faster but equally accurate rigid solver as the one currently used (Runge Kutta Adaptive), are needed for this.

A

Simulation and Spirometry Data

This section presents the measures obtained from spirometry and simulation on three subjects. Each subject was asked to breathe in a steady fashion in three different positions: standing, sitting and lying. For each position, they had to breathe normally (quiet breathing) and then more energetically (forced breathing) by making large breaths.

The resulting data was first processed to make any comparison possible as explained in chapter 4, section 4.2.

A.1. Subject 1

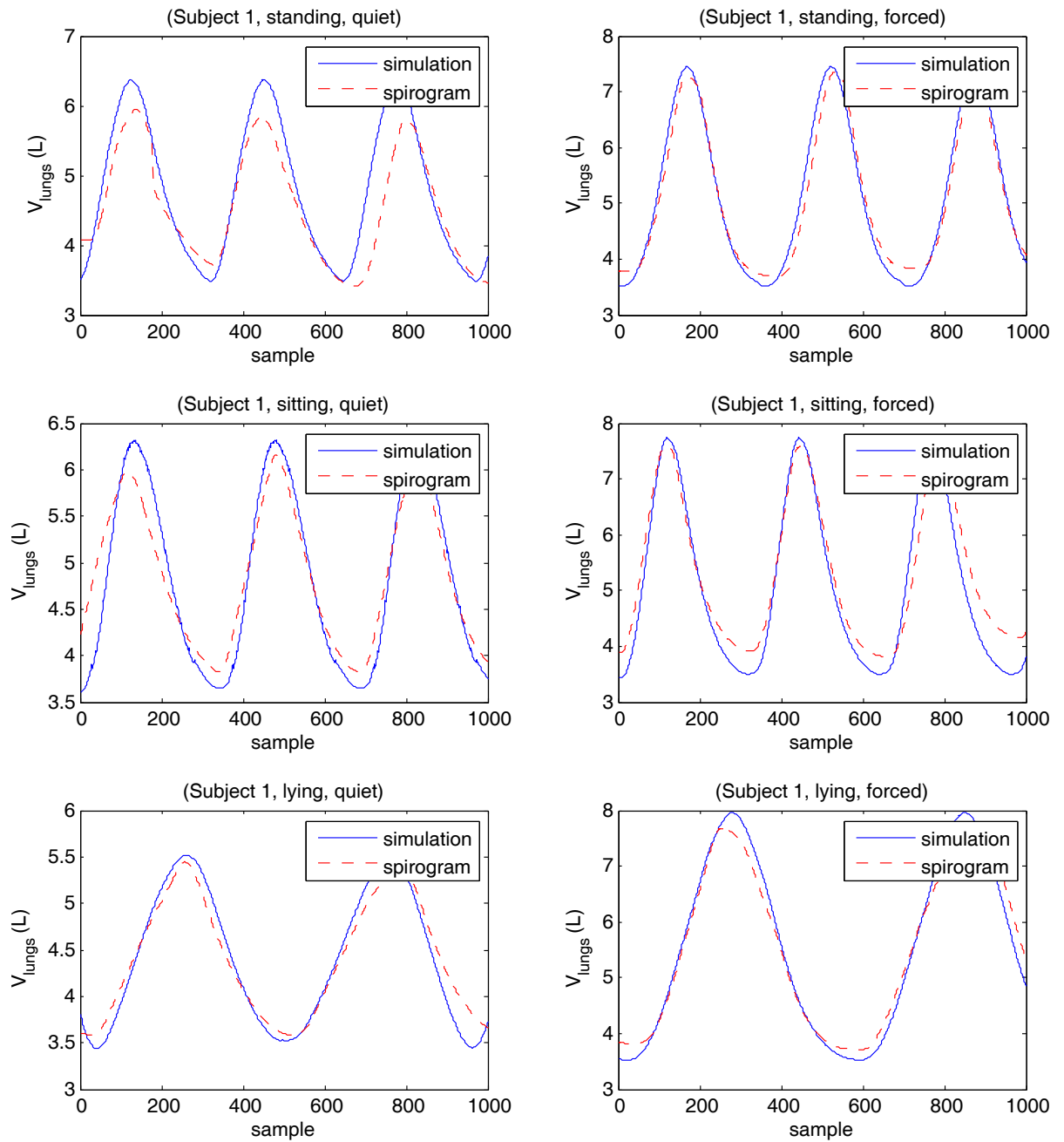


Figure A.1. Simulation and spirometry data from subject 1.

A.2. Subject 2

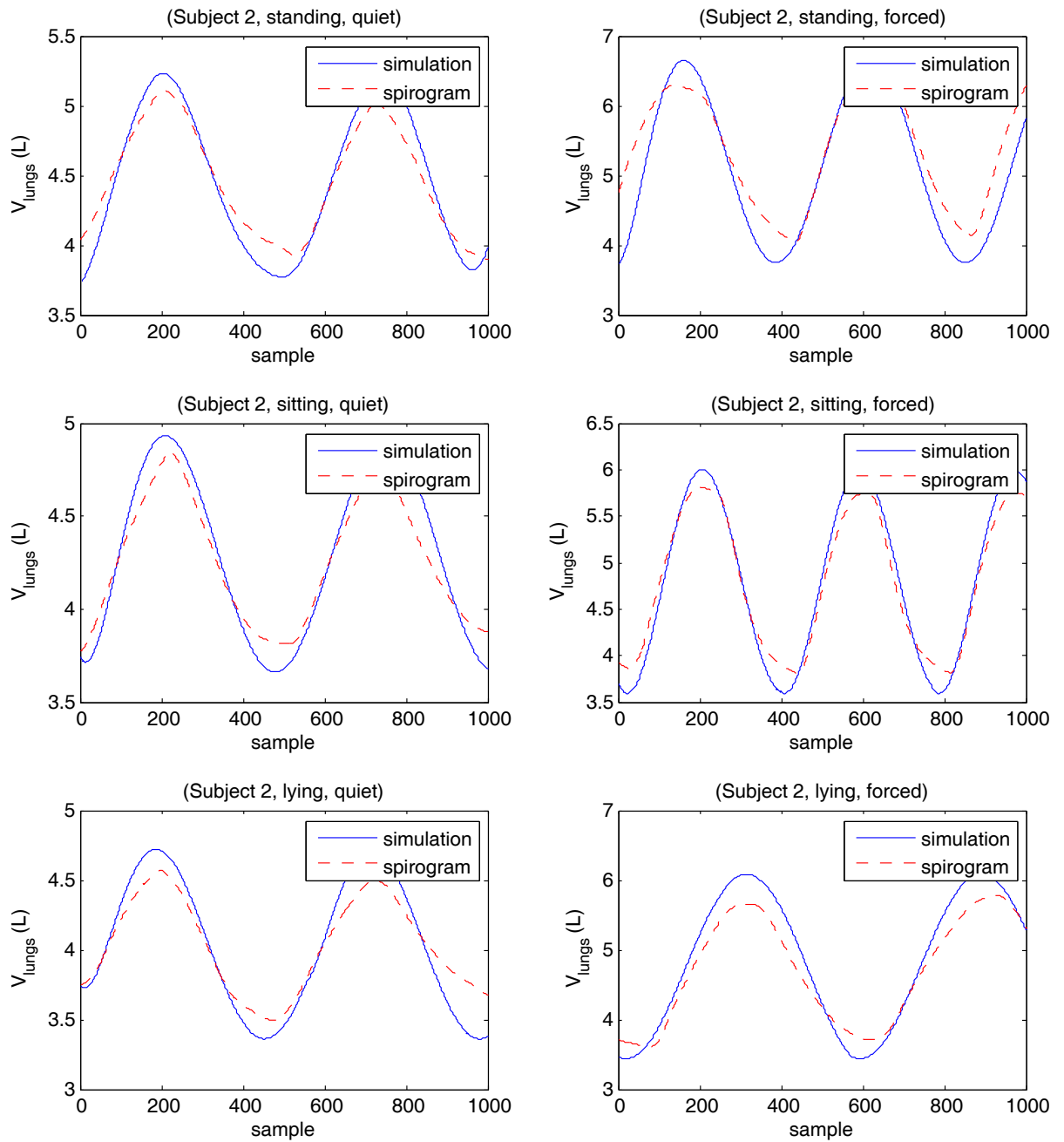


Figure A.2. Simulation and spirometry data from subject 2.

A.3. Subject 3

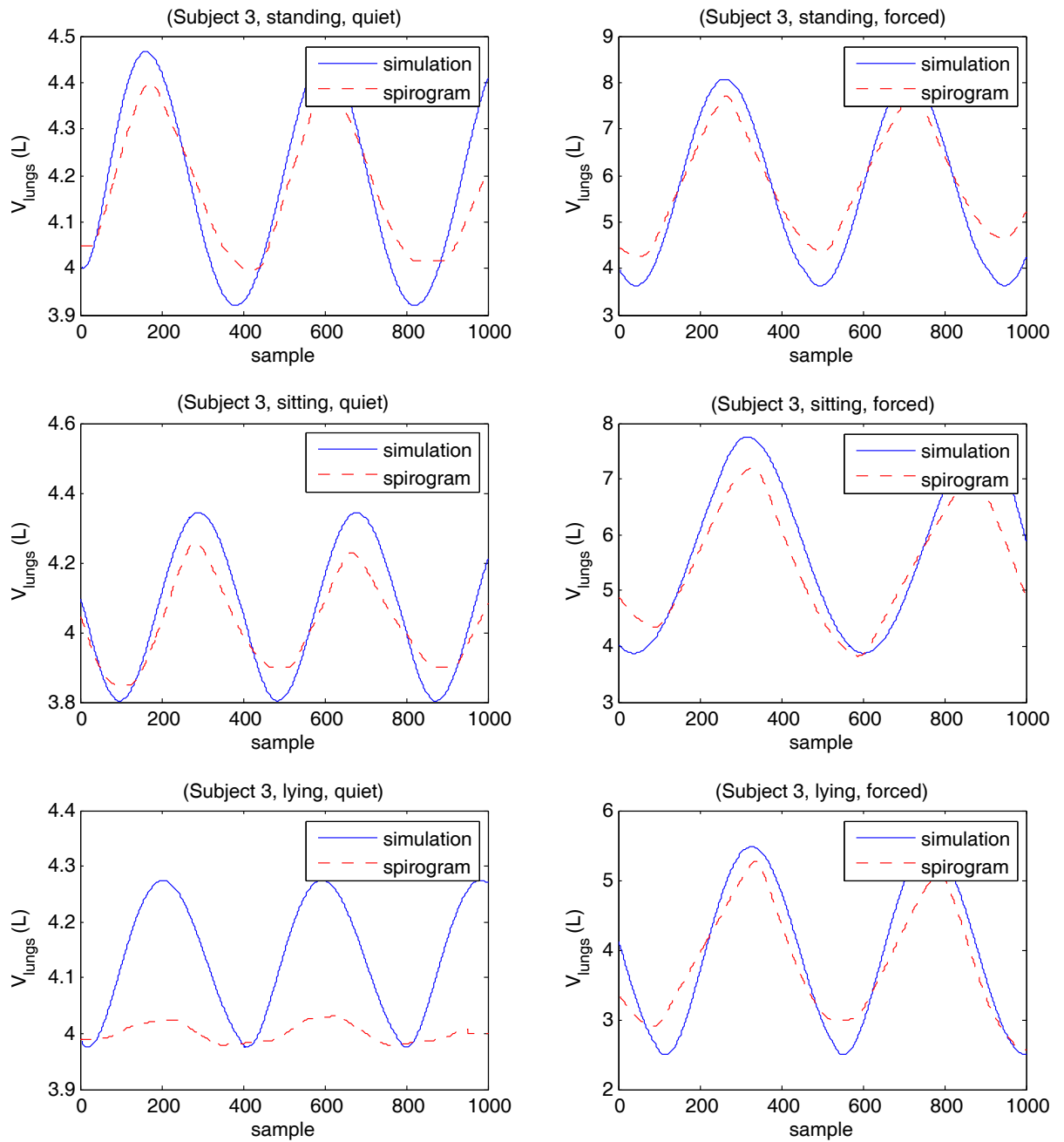


Figure A.3. Simulation and spirometry data from subject 3.

B

Bland-Altman Plots for Simulation and Spirometry Data

This section presents the Bland-Altman plots obtained from spirometry and simulation on three subjects. A blue dashed-dotted line for zero mean difference along with two red dashed lines at $\pm 1.96 \times SD_{diff}$ from the mean are included in the plots.

B.1. Subject 1

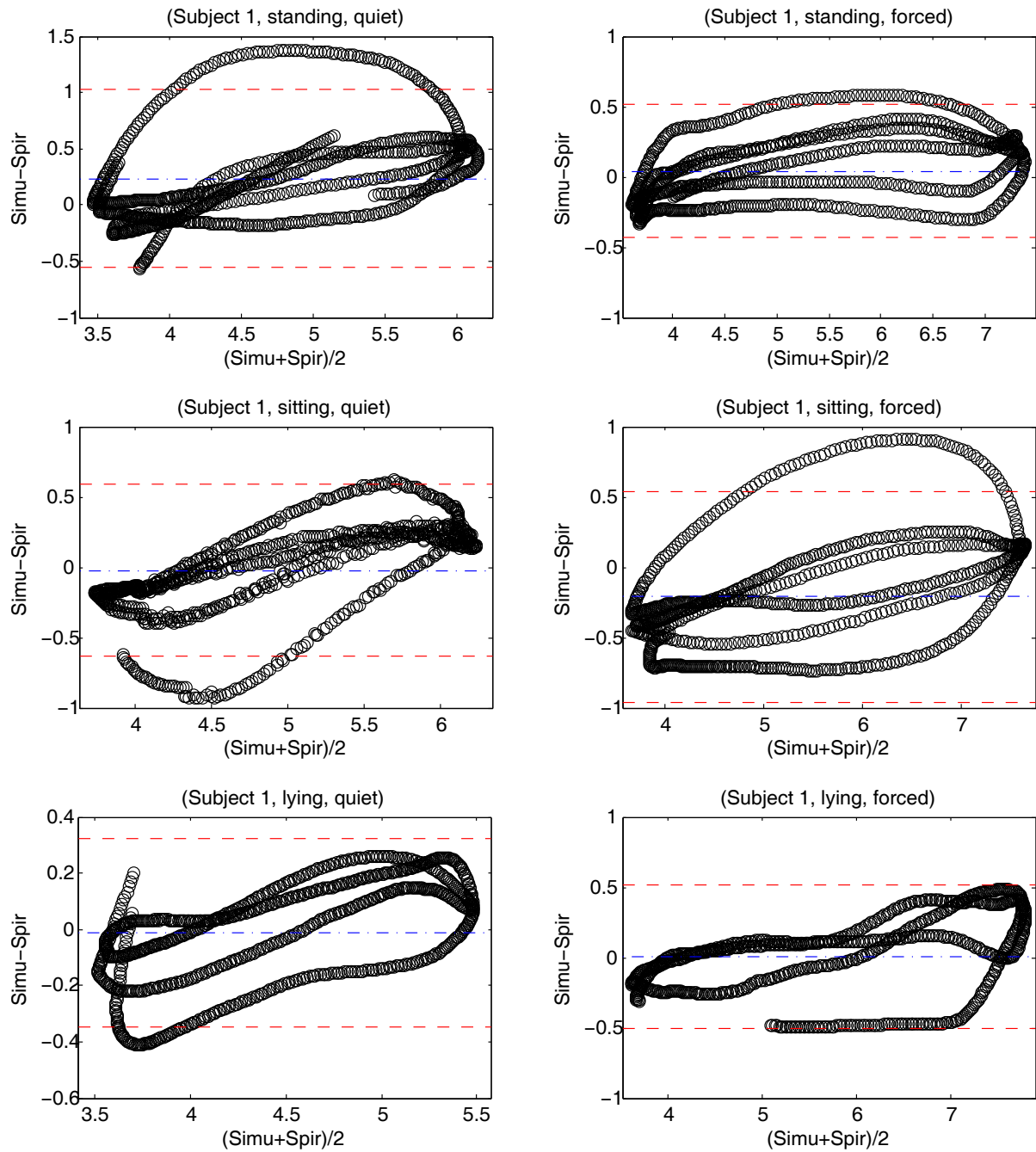


Figure B.1. Bland-Altman plots for simulation and spirometry data from subject 1.

B.2. Subject 2

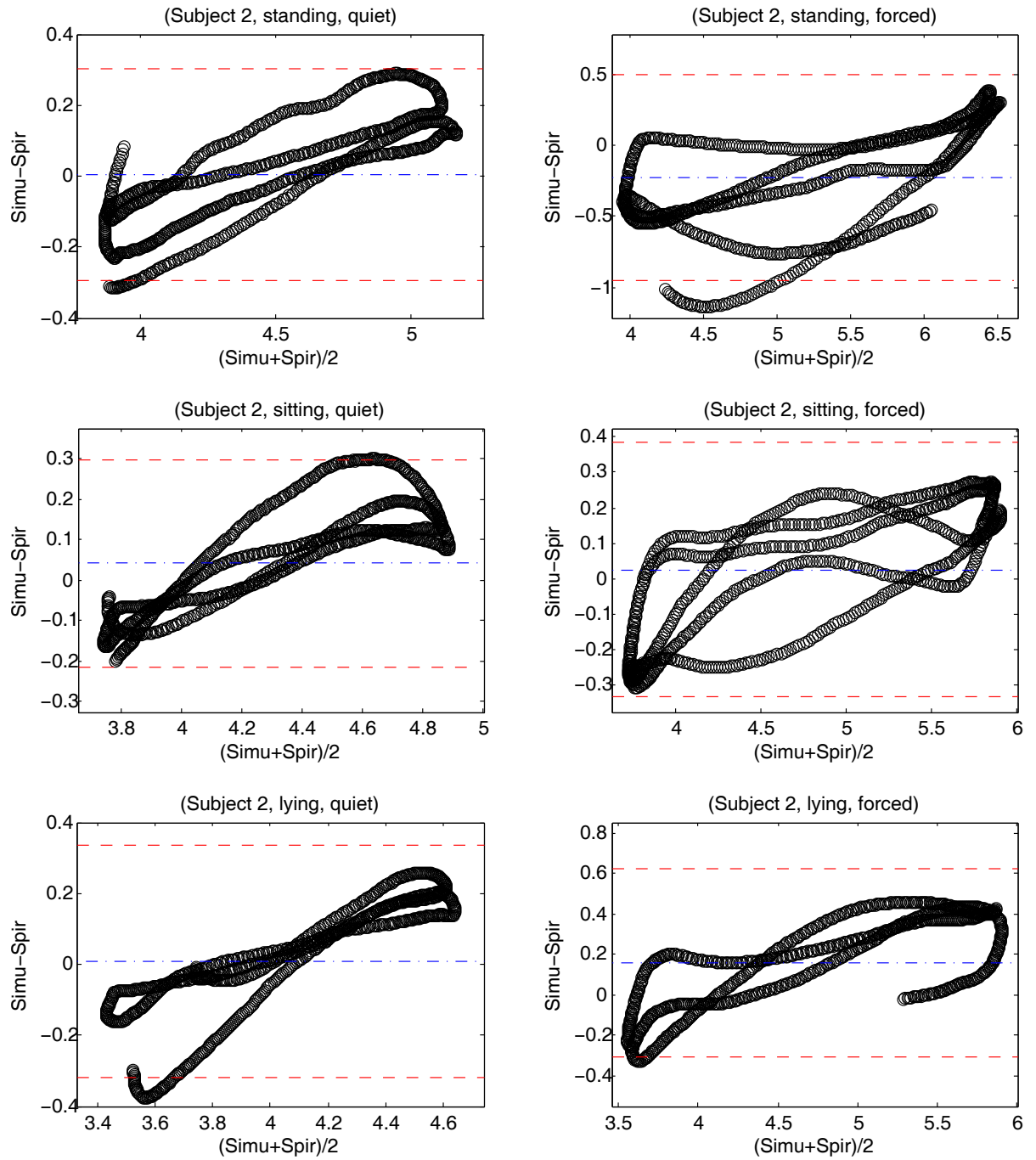


Figure B.2. Bland-Altman plots for simulation and spirometry data from subject 2.

B.3. Subject 3

B.3. Subject 3

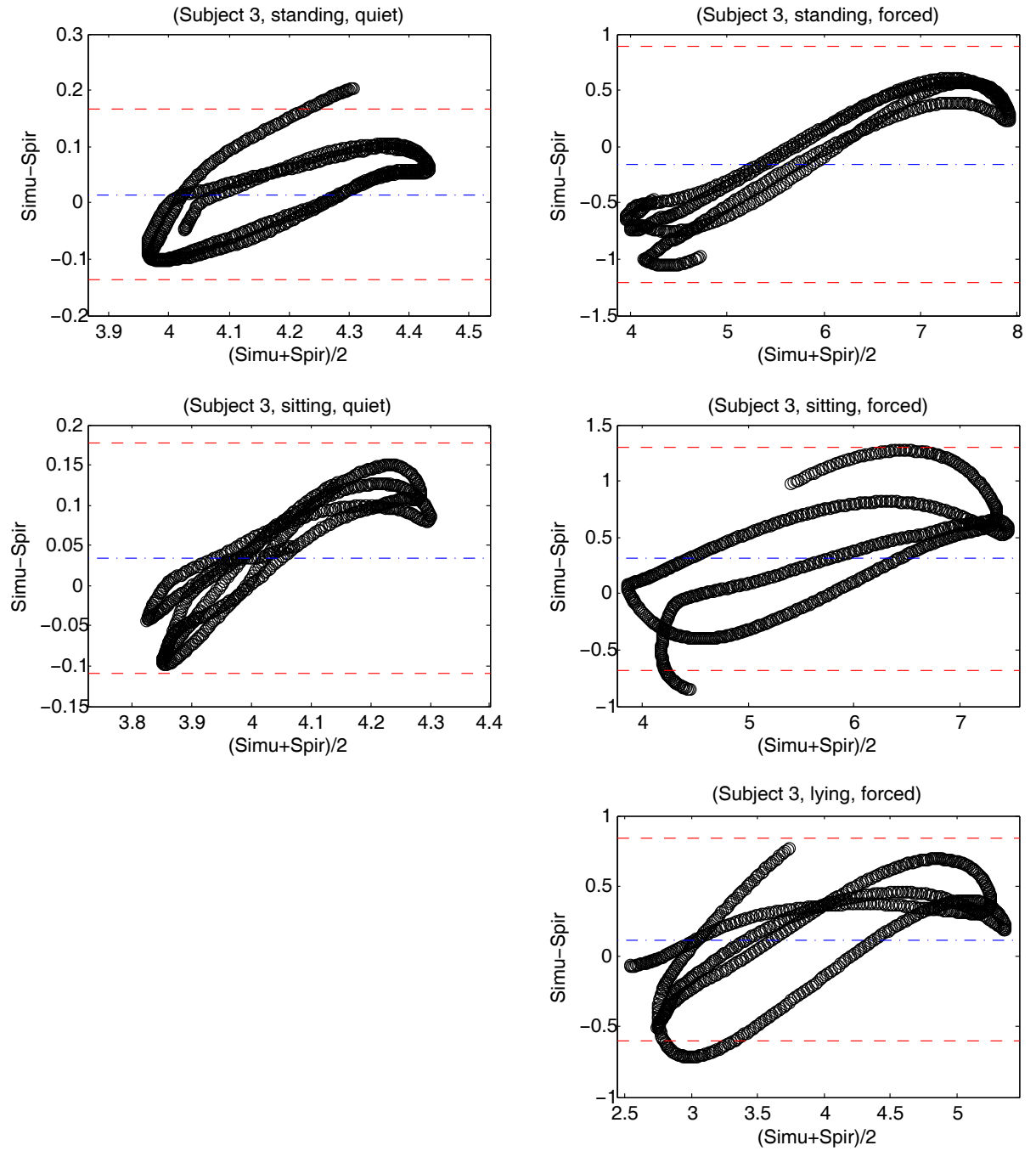


Figure B.3. Bland-Altman plots for simulation and spirometry data from subject 3.

Bibliography

- [1] T.J. Maldonado and J. Lasenby. Simulation of breathing for medical applications. In *ACM SIGGRAPH 2011 Posters*, SIGGRAPH '11, pages 7:1–7:1, New York, NY, USA, 2011. ACM.
- [2] W. de Boer, J. Lasenby, J. Cameron, R. Wareham, S. Ahmad, C. Roach, W. Hills, and R. Iles. SLP: A Zero-Contact Non-Invasive Method for Pulmonary Function Testing. In *Proceedings of the British Machine Vision Conference*, pages 85.1–85.12. BMVA Press, 2010. doi:10.5244/C.24.85.
- [3] S.H. Lee, E. Sifakis, and D. Terzopoulos. Comprehensive biomechanical modeling and simulation of the upper body. *ACM Trans. Graph*, 28(4):1–17, 2009.
- [4] V.B. Zordan, B. Celly, B. Chiu, and P.C. DiLorenzo. Breathe easy: model and control of simulated respiration for animation. In *Proceedings of the 2004 ACM SIGGRAPH/Eurographics symposium on Computer animation*, pages 29–37. Eurographics Association, 2004.
- [5] J. Carranza, C. Theobalt, M.A. Magnor, and H.P. Seidel. Free-viewpoint video of human actors. In *ACM SIGGRAPH 2003 Papers*, pages 569–577. ACM, 2003.
- [6] G. Monheit and N.I. Badler. A kinematic model of the human spine and torso. *Computer Graphics and Applications, IEEE*, 11(2):29–38, 2002.
- [7] S.H. Lee. *Biomechanical modeling and control of the human body for computer animation*. PhD thesis, UNIVERSITY OF CALIFORNIA, LOS ANGELES, 2008.
- [8] cgCharacter. Ultimate Human Model, 2008. <http://www.cgcharacter.com/ultimatehuman.html>.
- [9] K. Konno and J. Mead. Measurement of the separate volume changes of rib cage and abdomen during breathing. *Journal of Applied Physiology*, 22(3):407, 1967.

Bibliography

- [10] P.C. DiLorenzo, V.B. Zordan, and B.L. Sanders. Laughing out loud. In *ACM SIGGRAPH 2008 talks*, page 1. ACM, 2008.
- [11] P.C. DiLorenzo. *Breathing, laughing, sneezing, coughing: Model and control of an anatomically inspired, physically-based human torso simulation*. PhD thesis, UNIVERSITY OF CALIFORNIA, RIVERSIDE, 2009.
- [12] R. Veltkamp and B. Piest. A Physiological Torso Model for Realistic Breathing Simulation. *Modelling the Physiological Human*, pages 84–94, 2009.
- [13] Inc. Autodesk. Autodesk Maya 2010, 2010. <http://usa.autodesk.com/maya>.
- [14] Y. Nakamura, K. Yamane, Y. Fujita, and I. Suzuki. Somatosensory computation for man-machine interface from motion-capture data and musculoskeletal human model. *Robotics, IEEE Transactions on*, 21(1):58–66, 2005.
- [15] J. Sobotta, R. Putz, R. Pabst, A. Dhem, and A. Gouazé. *Atlas d'anatomie humaine*. Ed. médicales internationales, 1977.
- [16] F.H. Netter. *Atlas d'anatomie humaine*. Elsevier Masson, 2009.
- [17] H. Gray. *Anatomy of the human body*. Lea & Febiger, 1918.
- [18] K.L. Moore. *Clinically oriented anatomy*. Williams & Wilkins, 1992.
- [19] F.E. Zajac. Muscle and tendon: properties, models, scaling, and application to biomechanics and motor control. *Critical reviews in biomedical engineering*, 17(4):359, 1989.
- [20] R. Grzeszczuk and D. Terzopoulos. Automated learning of muscle-based locomotion through control abstraction. *Proceedings of ACM SIGGRAPH: Computer Graphics*, pages 63–70, 1995.
- [21] A. Jameson, W. Schmidt, E. Turkel, et al. Numerical solutions of the Euler equations by finite volume methods using Runge-Kutta time-stepping schemes. *AIAA paper*, 81:1259, 1981.
- [22] R.L. Drake, W. Vogl, and A.W.M. Mitchell. *Gray's anatomy for students*. Elsevier/Churchill Livingstone Philadelphia, 2005.
- [23] Q. Hamid, J. Shannon, and J. Martin. *Physiologic Basis of Respiratory Disease*. BC Decker Inc./ Hamilton, Ontario, Canada, 2006.
- [24] Syndrome du Défilé Thoraco Brachial. Scalene muscles, 2009. <http://sdtb.blogspot.com/>.
- [25] N.B. Slonim and L.H. Hamilton. *Respiratory physiology*. Mosby Inc, 1987.
- [26] D.T. Chen and D. Zeltzer. Pump it up: Computer animation of a biomechanically based model of muscle using the finite element method. In *Proceedings of the 19th annual conference on Computer graphics and interactive techniques*, pages 89–98. ACM, 1992.

Bibliography

- [27] X. Tu and D. Terzopoulos. Artificial fishes: Physics, locomotion, perception, behavior. In *Proceedings of the 21st annual conference on Computer graphics and interactive techniques*, pages 43–50. ACM, 1994.
- [28] G.K. Klute, J.M. Czerniecki, and B. Hannaford. Artificial muscles: actuators for biorobotic systems. *The International Journal of Robotics Research*, 21(4):295, 2002.
- [29] W.H. de Boer. Structured Light Plethysmography: A non-invasive method for pulmonary function testing using visible light. Master’s thesis, UNIVERSITY OF CAMBRIDGE, 2010.
- [30] S. Bennett. *Grid tracking in structured light plethysmography*. PhD first year report, UNIVERSITY OF CAMBRIDGE, 2011.
- [31] MakeHuman team 2001-2010. Make Human, 2010. <http://www.makehuman.org/>.
- [32] I. Baran and J. Popović. Automatic rigging and animation of 3d characters. *ACM Transactions on Graphics (TOG)*, 26(3):72–es, 2007.
- [33] R. Wareham and J. Lasenby. Bone Glow: An Improved Method for the Assignment of Weights for Mesh Deformation. *Articulated Motion and Deformable Objects*, pages 63–71, 2008.
- [34] J.P. Lewis, M. Cordner, and N. Fong. Pose space deformation: a unified approach to shape interpolation and skeleton-driven deformation. In *Proceedings of the 27th annual conference on Computer graphics and interactive techniques*, pages 165–172. ACM Press/Addison-Wesley Publishing Co., 2000.
- [35] A. Mohr and M. Gleicher. Building efficient, accurate character skins from examples. *ACM Transactions on Graphics (TOG)*, 22(3):562–568, 2003.
- [36] L. Kavan, S. Collins, J. Žára, and C. O’Sullivan. Skinning with dual quaternions. In *Proceedings of the 2007 symposium on Interactive 3D graphics and games*, pages 39–46. ACM, 2007.
- [37] J.A. Nelder and R. Mead. A simplex method for function minimization. *The computer journal*, 7(4):308, 1965.
- [38] Google and Inc. Zygote Media Group. Google Body, 2011. <http://bodybrowser.googlelabs.com>.
- [39] Inc. Zygote Media Group. Zygote Media Group 3D, 2011. <http://www.zygote.com>.
- [40] J.T. Sharp, N.B. Goldberg, W.S. Druz, and J. Danon. Relative contributions of rib cage and abdomen to breathing in normal subjects. *Journal of Applied Physiology*, 39(4):608, 1975.

Bibliography

- [41] D.G. Altman and J.M. Bland. Measurement in medicine: the analysis of method comparison studies. *Journal of the Royal Statistical Society. Series D (The Statistician)*, 32(3):307–317, 1983.
- [42] J. Martin Bland and D.G. Altman. Statistical methods for assessing agreement between two methods of clinical measurement. *The Lancet*, 327(8476):307–310, 1986.
- [43] C. Fogarty. Structured Light Plethysmography: A statistical comparison of tidal volume curves obtained using SLP and spirometry. Master’s thesis, HARVARD UNIVERSITY, 2011.
- [44] W. Nelson, Y.L. Tong, JK Lee, and F. Halberg. Methods for cosinor-rhythmometry. *Chronobiologia*, 6(4):305, 1979.
- [45] C. Alberola-López and M. Martín-Fernández. A simple test of equality of time series. *Signal processing*, 83(6):1343–1348, 2003.
- [46] M. Bisceglia, C.A. Galliani, C. Senger, C. Stallone, and A. Sessa. Renal cystic diseases: a review. *Advances in Anatomic Pathology*, 13(1):26, 2006.
- [47] I. Dimatteo, C.R. Genovese, and R.E. Kass. Bayesian curve-fitting with free-knot splines. *Biometrika*, 88(4):1055, 2001.
- [48] S. Behseta and R.E. Kass. Testing equality of two functions using BARS. *Statistics in medicine*, 24(22):3523–3534, 2005.
- [49] A. De Troyer. Mechanical role of the abdominal muscles in relation to posture. *Respiration physiology*, 53(3):341–353, 1983.